SEDIMENTOLOGY the journal of the International Association of Sedimentologists

Sedimentology (2023) doi: 10.1111/sed.13160

Processes controlling rare earth element distribution in sedimentary apatite: Insights from spectroscopy, *in situ* geochemistry and O and Sr isotope composition

SOPHIE DECRÉE*,† , ETIENNE DELOULE‡, RENATA BARROS*, JULIEN MERCADIER§, STEFAN HÖHN¶, CHANTAL PEIFFERT§ and JEAN-MARC BAELE**

**Royal Belgian Institute of Natural Sciences-Geological Survey of Belgium, Brussels B-1000, Belgium (E-mail: sophie.decree@naturalsciences.be)*

†The Mineral Resources Expert Group (MREG), EuroGeoSurveys, Brussels B-1000, Belgium

‡Université de Lorraine, CNRS, CRPG, Nancy F-54000, France

§GeoRessources Lab, Université de Lorraine, CNRS, Nancy F-54000, France

¶Department of Geodynamics and Geomaterials Research, Bavarian Georesources Centre, Institute of Geography and Geology, University of Würzburg, Würzburg D-97074, Germany

***Department of Geology and Applied Geology, University of Mons, Mons B-5000, Belgium*

Associate Editor – Nathan Sheldon

ABSTRACT

In phosphorites, the content and distribution of rare earth elements are linked to the environment of phosphogenesis. This paper focuses on the question of sources and processes controlling the rare earth element content of apatite from Belgian phosphorites formed during three major phosphogenic events in the Lower Palaeozoic, Late Cretaceous and Cenozoic. To constrain sources and processes, new data include petrological, mineralogical (including cathodoluminescence and Raman spectroscopy) and *in situ* trace element and Sr and O isotope analyses of apatite. Fluorapatite from Lower Palaeozoic P-rich conglomerates has the greatest rare earth element enrichment. It is affected by metamorphism that led to deformation of apatite nodules and formation of garnet porphyroblast inclusions. The role of Fe-oxyhydroxides in element scavenging is highlighted by some apatite nodules that maintain their primary middle rare earth element enrichment, while others are characterized by altered rare earth element patterns resulting from competition for these elements between co-crystallizing minerals during deformation. A systematic shift towards lower $\delta^{18}O$ and radiogenic Sr isotopic composition compared to contemporaneous seawater indicate interaction with ^{18}O-depleted meteoric fluids and a crustal component. By contrast, carbonate-rich fluorapatite from the Late Cretaceous phosphatic chalk mostly keeps its primary trace element and isotopic signatures (close to seawater), although an external rare earth element addition is noted, as well as rare earth element redistribution induced by diagenetic alteration. Cenozoic carbonate fluorapatite nodules mostly present flat rare earth element patterns that are indicative of a detrital influence. Slight changes in rare earth element distribution are assigned to post-depositional alteration, which also led to an increase in radiogenic Sr, with unchanged $\delta^{18}O$ compared to seawater. The methodology followed here efficiently helps in deciphering the processes that modified the chemistry of apatite in the frame of major phosphogenic events.

Keywords Apatite, Belgium, phosphogenesis, phosphorite, post-depositional processes, rare earth elements, Sr and O isotopes.

INTRODUCTION

Sedimentary phosphate deposits and occurrences are widely distributed in Europe (e.g. Decrée *et al.*, 2017). However, most of these deposits have not been reconsidered carefully for a few decades, especially regarding their geochemistry. However, the latter provides crucial information about the conditions that control the genesis of these deposits and helps to better constrain the sedimentological palaeoceanographic settings in which phosphorite forms. The rare earth element (REE) content and distribution in apatite give information about the environment during early diagenesis, which would be the preferential time for REE uptake of francolite (e.g. Jarvis, 1994; Shields & Stille, 2001; Chen *et al.*, 2015). Newly developed tools – such as *in situ* O and Sr isotope measurements on apatite – are helpful to decipher the complex history of phosphogenesis and constrain the post-depositional history of the phosphate deposit (i.e. interaction with diagenetic, meteoric or hydrothermal fluids or influence of metamorphic overprint; e.g. McArthur & Herczeg, 1990; Jarvis, 1994; Trappe, 2001; Brand *et al.*, 2011; Pufahl & Groat, 2017). Late diagenesis, metamorphism and epigenesis (for example, alteration) can affect the distribution of REE in apatite, which can complicate the interpretation of the REE signature.

This paper presents a petrographic and geochemical investigation of apatite from sedimentary and metasedimentary phosphate rocks of different ages, ranging from the Middle Cambrian to the Middle Miocene in Belgium. These case studies offer a unique opportunity to consider three major phosphogenic episodes occurring during the Lower Palaeozoic, the Late Cretaceous and the Cenozoic (e.g. Balson, 1980; Brasier, 1980; Notholt & Brasier, 1986; Parrish, 1990; Jarvis, 1992, 2006).

Cambrian (and late Precambrian) phosphorites are widespread on all continents, being generally associated with structural highs and periods of sea-level fluctuations. They likely testify to the greatest global phosphogenic episode in geological records (Notholt & Sheldon, 1986). Phosphorites of this age are commonly associated with glauconite, cherts, (pyrite-bearing) black shales and other lithologies suggesting anoxia and the presence of upwelling zones (e.g. Brasier, 1980; Parrish *et al.*, 1986; Álvaro *et al.*, 2016). The high organic productivity of upwelled waters would have been a probable source of phosphorus for these phosphorites (e.g. Álvaro *et al.*, 2016). In the Lower and Middle Cambrian, major phosphogenic cycles are typically associated with the early stage of a transgression, which is followed by a highstand or regression phase (e.g. Notholt & Brasier, 1986; Álvaro *et al.*, 2016). Reworking of primary phosphorites as turbidites would have led to phosphate concentration in cratonic basins along the Avalon Platform (e.g. Brasier, 1980).

The Late Cretaceous phosphogenic episode is well-expressed in the Tethyan series (Lucas & Prévôt-Lucas, 1995; Pufahl & Groat, 2017). The phosphorites of this age typically correspond to condensed sedimentation with periods of sediment starvation leading to the development of bioturbation and hardgrounds (Lucas & Prévôt-Lucas, 1995). The involvement of upwelled waters especially rich in P are thought to be one of the key factors leading to phosphogenesis (Pufahl & Groat, 2017). Among these Tethyan phosphorites, the Santonian–Lower Campanian and Lower Maastrichtian phosphatic chalk in Belgium, northern France and southern England appear to be somewhat disconnected from the South Tethyan phosphorite province. These phosphatic chalk deposits, which are the largest in size in Europe after the Lower Palaeozoic deposits in Estonia (Decrée *et al.*, 2017), accumulated on the shelving margins of basins along the London–Brabant Massif. Their formation would have benefited from unique sedimentological and palaeoecological conditions (Jarvis, 1992). The most striking difference with other deposits of the same age is that no major influence of upwelling was invoked (Jarvis, 1992). These deposits represent lowstand to early transgressive deposits after significant sea-level fall. They formed in a well-oxygenated, current-swept environment, and in a water depth between 70 m and a few hundred metres (Jarvis, 2006). Mineralization would have been a post-oxic process (Jarvis, 1992), with mixed redox conditions at a small scale (Jarvis, 1992).

The major episodes of phosphogenesis during the Neogene produced extensive phosphorites in

the Mediterranean area, the Middle East and South America, and during the Palaeogene on the eastern and western coast of North America, in Peru, South Africa and New Zealand (Riggs & Sheldon, 1990). They correlate with high sea-levels and largely testify to upwelling in marginal basins, with favourable sedimentological controls in these zones (Pufahl & Groat, 2017). The Palaeogene deposits are found in the inner continental shelf or in an epeiric sea setting (Parrish, 1990; Trappe, 2001) and their genesis can largely be compared to the Late Cretaceous phosphogenesis (Lucas & Prévôt-Lucas, 1995). Phosphogenesis during the Neogene presents however specificities. It took place in the context of a lower sea-level, compared with the earlier episodes of phosphogenesis. Nevertheless, the sea-level was probably high enough to enable currents with high productivities, due to cool temperature at the time and favourable continental positions (Parrish, 1990). The genesis of a few Miocene deposits, as the giant deposits of the south-eastern US continental shelf-coastal plain, is hardly reconcilable with the involvement of upwelled waters, and would relate to fluctuations of the eustatic sea-level, with change in climate and the Gulf Stream dynamics (Riggs, 1984).

Before performing *in situ* analyses – in order to investigate the composition of apatite from phosphorites formed during these events – petrographic observations using scanning electron microscope (SEM), cathodoluminescence (CL) and mineralogical characterization (Raman spectroscopy) were performed to highlight heterogeneities in phosphorites. *In situ* chemical and isotopic characterization include electron microprobe analyses (EMPA), laser ablation – inductively coupled plasma – mass spectrometry (LA-ICP-MS) to get *in situ* REE content and secondary ion mass spectrometry (SIMS) for O and Sr isotopic compositions. Although these isotope data provide essential information about sedimentary apatite deposition (e.g. Jarvis, 1994; Trappe, 2001), they have so far been scarcely used, whether for igneous or on sedimentary apatite (e.g. Emo *et al.*, 2018; Li *et al.*, 2018; Yang *et al.*, 2018; Decrée *et al.*, 2020a, 2022a,b, for Sr isotopic composition; and Žigaitė & Whitehouse, 2014; Chen *et al.*, 2016; Sun *et al.*, 2016; Zeng *et al.*, 2016; Wotte *et al.*, 2019; Yang *et al.*, 2020; Decrée *et al.*, 2020a; Edwards *et al.*, 2022, for O isotopic composition). By combining high spatial resolution trace element, O and Sr isotopic analyses, the processes involved in apatite formation (and the changes regarding its mineralogy and chemistry related to later processes) were investigated with unmatched precision.

GEOLOGICAL SETTING OF THE STUDIED PHOSPHORITES AND PHOSPHORUS-RICH ROCKS

This study aims to investigate phosphate deposits/occurrences representative of major phosphogenic events. Their distinct geological settings are detailed hereafter (see location in Fig. 1A).

The Early–Middle Cambrian phosphorites constitute the majority of phosphorites in Europe. They testify to the presence of a phosphogenic province connected to the Avalon and Baltic Platforms (Brasier, 1980; Notholt & Brasier, 1986). This province has been related to upwelling (and subsequent input of nutrients) along the western margin of Gondwana (Álvaro *et al.*, 2016). In Belgium, most of the phosphorites related to this event are located in the southern part of the Stavelot Massif. They are well-represented in the Grand Halleux borehole (Fig. 1B), in which Middle Cambrian rocks host at least 20 centimetric to decimetric (up to 20 cm thick) beds enriched in phosphate nodules (Revinian Rv1-2; Verniers *et al.*, 2001). The host rocks are made of an alternation of slaty quartzites and fine-grained slates/shales/schists containing organic matter (Franssen & Michot, 1969; Graulich, 1980; Verniers *et al.*, 2001). Interstratified volcanic tuffs are also present (Graulich, 1980; Geukens, 1999). Tholeiitic mafic dykes that are Ordovician to Silurian in age are also described in the series (Herbosch *et al.*, 2020). The P-rich beds are considered to represent conglomerate beds at the base of an arenaceous turbiditic sequence deposited in a pelitic environment, which developed in cratonic basins flanking the Avalon Platform (e.g. Brasier, 1980; Michot, 1980; Herbosch *et al.*, 2016). The sediments would originate from areas that are higher in terms of elevation where the detritic material was already sorted, and then transferred into areas of low topography (Michot, 1980). The Stavelot Massif was affected first by the Mid-Ordovician Caledonian and then by the Upper Carboniferous Variscan orogenies (Herbosch, 2021; and references therein). Taken as a whole, the epizonal peak metamorphic conditions estimated at the southernmost part of the Massif were between 300 to 400°C, and 100 to 200 MPa (data in Fielitz & Mansy, 1999).

Apart from the Lower Palaeozoic phosphorites of the Stavelot Massif, Middle Ordovician P-rich

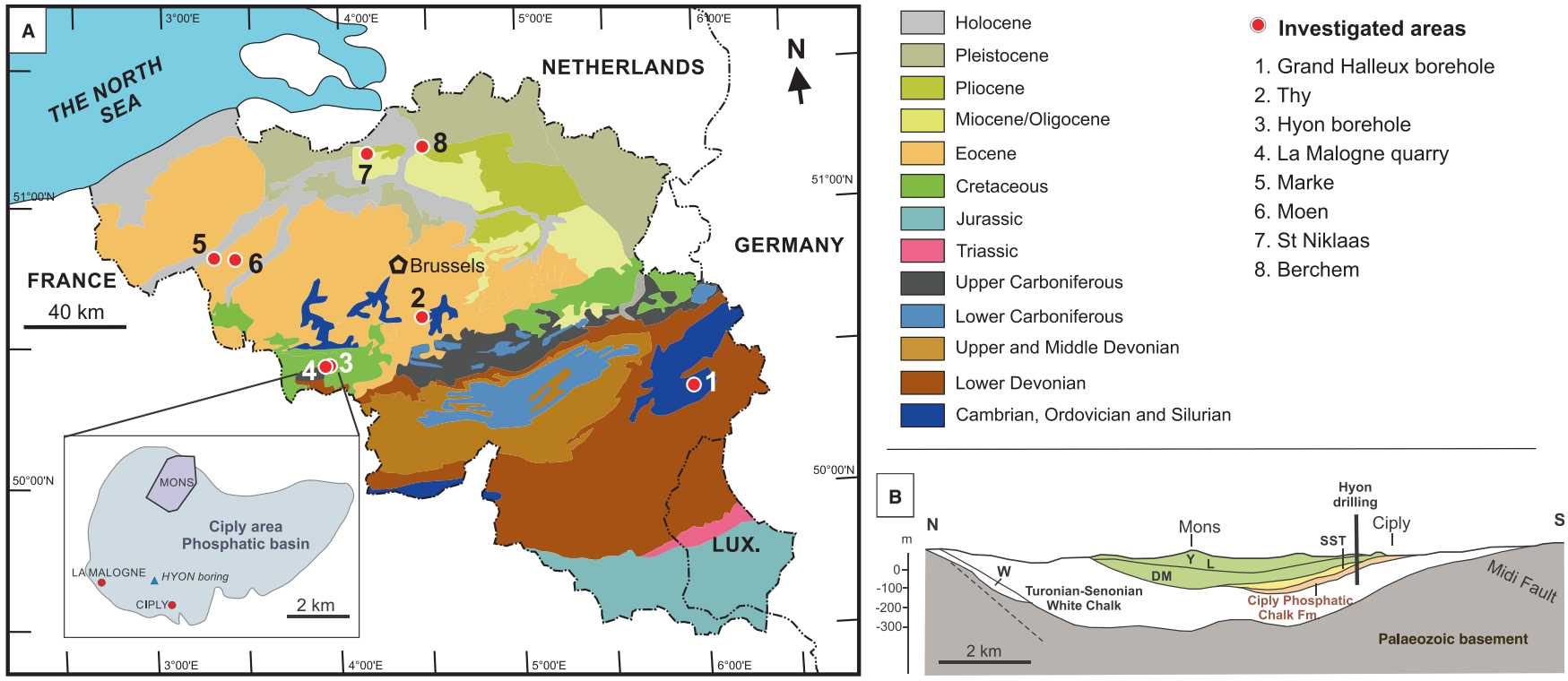

Fig. 1. (A) Location of the studied samples superimposed to the geological map of Belgium (Geological Survey of Belgium, 1996). The inset shows the location of sampling sites mentioned in the paper. (B) North–south geological section of the Mons Basin (modified from Robaszynski & Martin, 1988). W, Wealden facies; SST, Saint-Symphorien Tuffeau; DM, Danian and Selandian (former Montian); L, Thanetian (former Landenian); Y, Ypresian (from Robaszynski & Martin, 1988).

formations occur in the Brabant Massif (locality of Thy; Herbosch & Verniers, 2011; Fig. 1A), where a 2 m thick phosphatic and manganiferous conglomerate is interstratified with quartzite (de Magnée & Lambeau, 1965). In the conglomerate, black sub-rounded to ellipsoidal black nodules of phosphates are dominant. Other abundant non-sorted clasts made of siltstone to sandstone similar to the surrounding beds suggest the intraformational origin or proximal source for the conglomerate (de Magnée & Lambeau, 1965; Herbosch & Verniers, 2014). They are considered debris-flow deposits, considering the slump-related deformation features (pre-cleavage folds and faults) described by Debacker *et al.* (2009). Further analyses show that a south-dipping palaeoslope of regional extent should have been present during the Middle Ordovician in the southern part of the Brabant Massif (Debacker *et al.*, 2009). The rocks pertaining to the Brabant Massif show the overprint of a progressive and diachronous (*ca* 420 to 390 Ma; e.g. Debacker *et al.*, 2002; Linnemann *et al.*, 2012) low-grade metamorphism that ranges from epizone in the core to anchizone and diagenesis at the rim (Van Grootel *et al.*, 1997; Linnemann *et al.*, 2012). Most of this metamorphism can be related to a pre-kinematic burial, though a syn-kinematic contribution would explain the higher metamorphic degree observed (Debacker *et al.*, 2005).

An important sedimentary phosphate unit of Late Cretaceous age occurs throughout the Paris and Mons Basin (France and Belgium, respectively). It corresponds to a phosphogenic episode that prevailed at that time on the north-eastern margins of the Anglo-Paris Basin (Jarvis, 1992). The Mons Basin is the most significant phosphate deposit of this age, with estimates of the Maastrichtian Ciply Phosphatic Chalk Formation (CPC) resources reaching 960 million tons at a grade between 5% and 10% P_2O_5 (Robaszynski & Martin, 1988). This formation is a light brown phosphatic calcarenite that was deposited during the Middle–Late Cretaceous (Robaszynski & Martin, 1988). It forms a lens-shaped body with a thickness that varies from several metres at the southern margin to more than 70 m at the centre of the lens (Fig. 1B and C). It is marked at its base by a conglomeratic bed containing phosphatic pebbles (the Cuesmes Conglomerate) on the margin of the basin (Robaszynski & Martin, 1988). The phosphatic calcarenite of the Mons Basin represents a cycle of transgression–regression in an epicontinental sea, where phosphates would form during transgressive episodes followed by reworking/winnowing driven by sea-level fluctuation (Jarvis, 1992; Jacquemin, 2020). A recent Quaternary weathering process was responsible for the development of cryptodolines at La Malogne (western margin of the Mons Basin; Fig. 1B). The latter is controlled both by the regional tectonic setting and the characteristics (lithology and thickness) of the sedimentary cover overlying the calcarenites (De Putter *et al.*, 1999). Their infillings are enriched in phosphates compared to the host rock and relate to the selective dissolution of carbonates during the Quaternary (Quinif *et al.*, 1997; De Putter *et al.*, 1999).

Last major phosphogenic events occurred during the Cenozoic. In the North Sea, these episodes of phosphogenesis correspond to times of high sea-level in a period of eustatic sea-level fluctuation (Balson, 1980). Phosphates have been deposited during all major transgressions, likely in connection with regional subsidence. During the Eocene and the Oligocene, eustatic rise of the sea-level resulted in increasing exchange between the North Sea and oceanic waters, with subsequent increasing influence of upwelling on biological productivity (Lovell, 1986). High productivity under shallow marine conditions in an environment connected with the Atlantic Ocean is also evoked during the Miocene of the North Sea (Van den Bosch *et al.*, 1975; Louwye, 2005). However, a significant influence of upwelling on phosphogenesis is debated, considering the relative (too) shallow marine conditions (e.g. Riggs & Sheldon, 1990). In this context, even the role of upwelled waters in the genesis of several larger Cenozoic phosphorites is questioned (Riggs, 1984; Trappe, 2001). One of the most obvious effects of rising sea-level on phosphogenesis is observed in the Late Palaeocene–Early Eocene (Balson, 1980). In Belgium, this event is highlighted by an Early Ypresian phosphate nodule bed (Balson, 1980) that is widespread throughout East and West Flanders (as in Marke and Moen which are shown in Fig. 1; Van Marcke *et al.*, 2005). Another phosphogenic event is emphasized by a Middle Oligocene phosphorite bed of about 25 to 30 cm, occurring *ca* 3 m below the base of the Boom Clay Formation (as at St Niklaas; Fig. 1). Its lateral extent is very limited, being smaller than 5 km (Marquet & Herman, 2012). Abundant phosphorite concretions are observed in the North Sea area (Balson, 1980), as exemplified by the phosphatic bed encountered in the Middle Miocene Antwerpen Sands (as in Berchem, Fig. 1; Louwye, 2002).

Table 1. Succinct description of the examined P-rich rocks from Belgium.

Locality	Age	Sample name	Macroscopic description
Grand Halleux (boring)	Middle Cambrian (Series 3)	GH2457	Phosphate nodules (millimetre-size) in slate–quartzite intercalations
		GH2666	Phosphate nodules (millimetre-size) in slate–quartzite intercalations
		GH2743	Phosphate nodules (millimetre-size) in a silty porphyroclast comprised in slate–quartzite intercalations
		GH2952	Deformed/elongated phosphate nodules (millimetre-size) and thin P-rich laminae in slate–quartzite intercalations
Thy-le-Chateau	Middle Ordovician	THY1	Conglomeratic bed: phosphate nodules (millimetre-size) with inclusions of garnet in a silty matrix
		THY2	Conglomeratic bed: phosphate nodules (millimetre-size) with inclusions of garnet in a silty matrix, stained with Fe-oxides
Hyon (boring)	Late Cretaceous	Hb56.76	Matrix-supported carbonate rock with silt-sized and sand-sized peloidal phosphatic grains
		Hb79.06	Matrix-supported carbonate rock with silt-sized and sand-sized peloidal phosphatic grains
		Hb90.2	Grain-supported carbonate rock with peloidal phosphatic grains
La Malogne	Late Cretaceous	LM1	Matrix-supported carbonate rock with silt-sized and sand-sized peloidal phosphatic grains
		LM4	Weakly consolidated conglomeratic carbonate rock with abundant phosphatic pebbles
	Quaternary	LM3	Unconsolidated to very weakly consolidated silt-sized and sand-sized peloidal phosphatic grains
Marke, Kockelberg	Early Eocene	MA	Centimetre-size phosphate nodule in a glauconitic bed
Moen, Bossuit Canaal		MO	Centimetre-size phosphate nodule in a glauconitic bed
Sint Niklaas	Lower Oligocene	STN1	Centimetre-size phosphate nodule in the 'Boom clay'
		STN2	Centimetre-size phosphate nodule in the 'Boom clay'
Berchem	Middle Miocene	BERCH1	Centimetre-size phosphate nodule in the 'Sables d'Anvers', Berchem Formation
		BERCH2	Centimetre-size phosphate nodule in the 'Sables d'Anvers', Berchem Formation

MATERIAL AND METHODS

Thirty samples have been investigated from a petrographic and mineralogical point of view for this study (Table 1). A selection of these specimens is presented in Fig. 2. Most of the samples come from the Grand Halleux borehole (171 W276; Fig. 1) stored at the Geological Survey of Belgium (GSB), Royal Belgian Institute of Natural Sciences (RBINS) and from the Hyon borehole (Fig. 1) that is part of the University of Mons (UMONS) collections. Lower Oligocene P-rich rocks were also found in the RBINS collections, whereas Middle Ordovician, Early Eocene and Middle Miocene apatite nodules were collected in the field by S. Decrée, E. Steurbaut (RBINS) and O. Lambert (RBINS), respectively. Phosphate-rich rocks from the La Malogne quarry (Fig. 1) were collected in

the field. The petrographic analysis (Figs 3 and 4) was based on optical microscopy and scanning electron microscopy (SEM) using a Quanta 20 ESEM (FEI, Hillsboro, OR, USA), with energy-dispersive spectroscopy (Apollo 10 Silicon Drift EDS (energy dispersive spectroscopy) detector; EDAX, Pleasanton, CA, USA) at RBINS. Cathodoluminescence (CL) studies (Figs 3, 4 and 5) were performed at UMONS using a cold-cathode CL unit model Mk5 operated at 15 kV beam voltage and 500 μA current (Cambridge Image Technology Limited, Hatfield, UK). The surface of the unfocused electron beam on the sample was 12 × 4 mm, resulting in a current density of about 10 $\mu A/mm^2$. CL spectra were recorded with a CITL optical spectrometer model OSA2 (Cambridge Image Technology Limited) allowing acquisition from 350 to 1100 nm at 3.7 nm spectral resolution. Spectra were acquired and processed using Spectragryph optical spectroscopy software (https://www.effemm2.de/spectragryph/). A dark spectrum, i.e. a spectrum of the stray light in the CL chamber, was systematically subtracted from the experimental spectrum. Spectral CL images of the Nd^{3+} emission were collected by inserting in the light path an optical bandpass filter with a transmission curve centred at 880 nm and 50 nm wide (full width at half maximum). Such spectral CL imaging enhances the details of the distribution of the apatite activated by light REE (LREE), which is especially useful when apatite luminescence is overwhelmed by the intense luminescence of calcite and feldspars. In addition, Nd^{3+} emits in the near infrared region of the spectrum and is therefore not visible in colour CL images. Raman spectroscopy was performed at RBINS to investigate the fluorescence induced by the REE. A 532 nm (green) laser Raman spectrometer (Senterra, Bruker, Billerica, MA, USA; Olympus BX51, Olympus, Tokyo, Japan) was used. The spectra were acquired using a 2 mW excitation power, 5 × 30 s integration time and with a 50 μm spectrometer slit. They were processed using Spectragryph optical spectroscopy software. X-ray diffraction (XRD) was performed at RBINS. The powdered samples were analysed using a diffractometer PANanalytical Empyrean (copper anode with CuKα λ: 15418 Å, a nickel filter, 45 kV and 40 mA detector X'Celerator; Malvern Panalytical, Malvern, UK). The sample powders are first loaded in a steel holder and measured in a Bragg-Brantano configuration. The studied angles were between 6 and 69 degrees 2Θ. The semi-quantitative interpretation is done using Visual Crystal 6 software.

The main results of the petrographic and mineralogical investigations are presented in Table S1. Where possible, different types of analyses [electron micro-probe analysis (EMPA) and laser ablation – inductively coupled plasma – mass spectrometry (LA-ICP-MS)] have been performed on the same spot or in very close proximity to that spot. Quantitative micro-analysis of major elements (Table S2) was performed using a JXA 8800 L electron microprobe (JEOL Limited, Tokyo, Japan) at the Institute of Geography and Geology, University of Würzburg (Germany). It was operated at 15 kV and 20 nA, with a beam diameter of 10 μm. This microprobe is equipped with four wavelength-dispersive (WDS) spectrometers and standard LDE1, TAP, PET and LIF crystals. The following standards were used for calibration of the EPMA: LiF for F; Fe_2O_3 for Fe; $SrSO_4$ for Sr; $MnTiO_3$ for Mn; MgO for Mg; $BaSO_4$ for S and Ba; albite for Na; vanadinite for Cl; apatite for P and Ca; and andradite for Si. The Lα line was used for the measurements of Sr and Ba, and the Kα line for all other elements. The lower limit of detection is typically better than 0.05 wt.%. For each analytical spot, the relatively mobile elements F and Na were analysed first in order to prevent their potential loss in the course of the analysis. A correction for excess F due to third-order interference of P Kα on F Kα was applied. Excess F was estimated at about 0.35% based on 15 measurements of F Kα in a phosphate that does not contain F (reference monazite at University of Würzburg). The measurements yielded a mean of 0.040% 'fake' F per % P. A similar value (0.045%) was obtained by Potts & Tindle (1989). Note that grain orientation and anisotropic ion diffusion can also have a substantial influence on the measurement of F with the electron microprobe (e.g. Stormer *et al.*, 1993; Goldoff *et al.*, 2012).

Laser ablation – inductively coupled – mass spectrometry was performed at GeoRessources (Nancy, France), with a ESI NWR193 excimer laser (ArF, 193 nm; Kenelec Scientific, Mitcham, Australia) coupled to a: (i) primary viewing system, full HD 1080p digital camera with 15× to 60× objective to camera magnification; (ii) secondary viewing system, 25 mm field of view for macro navigation; (iii) three high-intensity, LED light sources (coaxial, ring and transmitted) for sample observation and laser beam focusing onto the sample; and (iv) an Agilent 8900 triple quadrupole ICP-MS used in no-gas mode

(Agilent Technologies, Santa Clara, CA, USA). These data are presented in Table S3. The LA-ICP-MS system was optimized to have the highest sensitivity for all elements (from ^{7}Li to ^{238}U), ThO/Th ratio <0.4% and Th/U ratio of *ca* 1 by ablating the NIST standards. Samples were ablated with a laser spot size of 30 μm to avoid mixing between the different zones observed in the apatite crystals. A fluence of *ca* 6 J/cm^2 and a repetition rate of 5 Hz were used. The carrier gas used was helium (0.45 l/min), which was mixed to argon (0.65 l/min) gas before entering the ICP-MS. The ICP-MS settings were; ICP RF Power at 1550 W, cooling gas (Ar) at 15 l/min, auxiliary gas (Ar) at 0.7 l/min, make-up gas (Ar) at 0.5 l/min and dual detector mode used. For each analysis, acquisition time was 30 s for background, 40 s for external standards [NIST SRM 610, NIST SRM 612 and NIST SRM 614 silicate glasses (see Jochum *et al.*, 2011 for concentrations)] and 40 to 50 s for apatite. The analytical procedure for the two analytical sessions was as follows; two analyses of NIST SRM 614, two analyses of NIST SRM 612, two analyses of NIST SRM 610, analyses of the apatites (series of *ca* 20 analyses separated by the analysis of a series of one NIST SRM 614, one NIST SRM 612 and one NIST SRM 610), two analyses of NIST SRM 614, two analyses of NIST SRM 612 and two analyses of NIST SRM 610. The external standard was NIST SRM 610 and ^{44}Ca was used as an internal standard. NIST SRM 614 and NIST SRM 612 silicate glasses were analysed and considered as cross-calibration samples to control the quality of the analyses (precision, accuracy and repeatability) and to correct the possible drift during the analytical session. Calcium contents in apatite were measured before LA-ICP-MS analyses using an electron microprobe (JEOL JXA 8800 L) at the University of Würzburg, Germany, to check the overall homogeneity of the apatite grains. The Ca concentration used for internal standardization was the content measured using the electron microprobe presented in Table S2. Consequently, 12 Ca concentrations have been used. The following isotopes were measured: ^{29}Si, ^{44}Ca, ^{45}Sc, ^{51}V, ^{85}Rb, ^{88}Sr, ^{89}Y, ^{90}Zr, ^{93}Nb, ^{137}Ba, ^{139}La, ^{140}Ce, ^{141}Pr, ^{146}Nd, ^{147}Sm, ^{153}Eu, ^{157}Gd, ^{159}Tb, ^{163}Dy, ^{165}Ho, ^{166}Er, ^{169}Tm, ^{172}Yb, ^{175}Lu, ^{178}Hf, ^{181}Ta, ^{208}Pb, ^{232}Th and ^{238}U. Acquisition times were 0.01 s for all isotopes except rare earth elements, which were measured with 0.02 s. Total cycle time was 531 ms. The precisions were better than 10% for all rare earth elements. Data treatment was completed using the software 'Iolite' (Paton *et al.*, 2011), following Longerich *et al.* (1996) for data reduction.

Oxygen (O) and strontium (Sr) isotope compositions were obtained using a IMS 1280 HR2 ion microprobe (Cameca, Gennevilliers, France) (secondary-ion mass spectrometry, SIMS) at CRPG Nancy (data presented in Table S4). Oxygen isotopic ratios were measured with a Cs + primary ion beam of 3.5 nA focused on a 15 μm diameter area and with the electron gun used for the charge compensation. The negative secondary ions were measured with a mass resolution of 3000 (M/ΔM) with an energy slit of 35 eV. Before each measurement, the sample was pre-sputtered for 90 s with a beam rastering on 15 μm to clean up the sample surface, then the secondary beam was automatically centred in the field aperture and contrast aperture. The measurements were made on Faraday collectors in multi-collection mode with a counting time of 150 s, with an internal precision of about 0.1‰. The instrumental mass fractionation was determined on the reference apatite Durango ($\delta^{18}O$ = 9.4‰; Trotter *et al.*, 2008), measured before and after each sample. Durango apatite is a fluorapatite with a composition overall similar to the measured samples (Marks *et al.*, 2012). The external 1σ precision on the reference material ranges in between 0.15‰ and 0.20‰, with an instrumental isotopic fractionation on the $^{18}O/^{16}O$ ratio ranging in between 3‰ and 4‰. The reported errors are the quadratic sum of the internal error and of the reference material external error. The measured ratios are expressed in $\delta^{18}O$ values relative to the Standard Mean Ocean Water (SMOW) value. The Sr isotope ratios were measured with the radio-frequency (RF) plasma source producing an O-primary beam accelerated at 13 kV and focused on the sample surface to produce a 10 μm spot with an intensity between 10 nA and 40 nA, depending on the Sr content of the samples. Positive secondary ions were extracted with a 10 kV potential. The positive secondary ions were measured at a mass resolution of 20 000 (M/ΔM), to remove almost all of the isobaric interference on the Sr isotopes. Indeed, at this mass resolution, all of the major Ca^{2+} overlapping masses are resolved, except for ^{87}Rb overlapping on ^{87}Sr, that needs to be corrected. The measurements were performed in mono-collection in ion counting mode, by peak switching over the masses 83.7 for the background measurement, ^{84}Sr, $^{84}Ca^{2+}$, ^{85}Rb, ^{86}Sr, ^{87}Sr and ^{88}Sr, with counting time of 3 s, 3 s, 8 s, 16 s, 16 s and 8 s, respectively. Each measurement consisted of 24 to 30 cycles (30 to

40 mn). The secondary ion intensity on ^{88}Sr was set in between 10^5 to 3×10^5 by adjusting the primary ion beam intensity. The instrumental mass fractionation between Sr isotopes was corrected for a $^{86}Sr/^{88}Sr$ ratio of 0.1194. The ^{87}Rb isobaric interference on ^{87}Sr was corrected for the measured ^{85}Rb count rate, a $^{87}Rb/^{85}Rb$ ratio of 0.3825, and the instrumental mass fractionation measured for Sr. The reported errors include the errors on the measured $^{87}Sr/^{86}Sr$, $^{86}Sr/^{88}Sr$ and $^{85}Rb/^{86}Sr$ ratios. The errors range from 0.3 to 2.0‰ (1σ), depending on the Sr and Rb contents. The Sr contents were calculated by using the measured $^{86}Sr/^{84}Ca^{2+}$ ratio and the Durango apatite ($^{87}Sr/^{86}Sr = 0.7063$; Yang *et al.*, 2014) as a reference material. The initial isotopic ratios have been calculated on the basis of the estimated formation age of the phosphorite (Table S4).

RESULTS

Brief macroscopic and mineralogical description

In the Middle Cambrian phosphorite beds (samples GH2457, GH2666, GH2743 and GH2952), the dark grey sub-rounded to ellipsoidal apatite nodules are found in association with black quartz nodules in sulphide-rich pluricentimetric beds hosted in a shale matrix made of chlorite and quartz with minor carbonates (see XRD; Table S1). The nodules, which reach a few millimetres in size (Fig. 2A and B), are variably deformed (elongated/flattened) and commonly broken. Locally, the P-rich silty beds themselves are fissured/brecciated (upper part in Fig. 2B). In the most extreme cases, these beds can even be reworked as sub-rounded lithoclasts, as shown in Fig. 2B (lower part). In these lithoclasts, the apatite nodules seem to be less deformed than the other facies. In the most deformed samples, apatite locally forms thin lenses/layers (white arrows in Fig. 2A). In the Middle Ordovician matrix-supported phosphate-rich beds, apatite occurs as black sub-rounded ellipsoidal nodules that are typically <1 cm in length and commonly brecciated/reworked (Fig. 2C; samples THY1 and THY2).

The Late Cretaceous Phosphatic Chalk Formation is a phosphatic calcarenite, the colour of which is directly related to the phosphate content (the darker brownish colour, the higher the phosphate concentration; Fig. 2D; samples Hb56.76, Hb79.06, Hb90.2, LM1). The apatite content varies distinctly from a few percent to about 10% in the richer formations (see XRD data, Table S1). At the margin of the basin (La Malogne locality), a weakly consolidated conglomerate with abundant phosphatic pebbles and calcareous cement is also encountered (Fig. 2E, sample LM4). Phosphate-enriched karstic pockets (cryptodolines) are also present in the same zone. They are made of silt-sized and sand-sized peloidal phosphatic grains. Carbonates are almost totally absent in these pockets due to karstic processes (leaching). Instead, they are enriched in phosphates, Fe-oxides and clays (sample LM3; XRD data, Table S2).

In the phosphate-rich beds of the Early Eocene (samples MA and MO), the Lower Oligocene (samples STN1 and STN2) and the Middle Miocene (samples BERCH1 and BERCH2), the brown to black apatite nodules investigated (Fig. 2F and G) are mostly centimetric in size and sub-rounded to angular (some of them are seemingly brecciated). Phosphatic concretions also fill fossil moulds (Fig. 2F). These Cenozoic apatite concretions contain numerous inclusions that are predominantly made of quartz, glauconite and feldspar (XRD data, Table S1). The host rocks of the apatite nodules have not been investigated for the present study, but concise descriptions are given by other authors. According to Van Marcke *et al.* (2005), the Early Eocene phosphorite is made of a very fine silty clay, rich in pyrite with isolated apatite and carbonate nodules. The Lower Oligocene P-rich layer comprises coarse sand with phosphatic nodules, pebbles, grains or concretions (indurated burrows among others) (Marquet & Herman, 2012), whereas the Middle Miocene phosphatic bed consists of sands with apatite nodules, bones and shark teeth (Louwye *et al.*, 2010).

Petrography and mineralogy

Middle Cambrian and Middle Ordovician phosphorus-rich rocks

In the Middle Cambrian turbiditic horizons, apatite occurs as isolated sub-rounded to ellipsoidal nodules from a few hundreds of micrometres to a few millimetres long (Fig. 3A to C). They are commonly slightly deformed, flattened and show evidence of brecciation. The nodules are heterogenous and predominantly contain inclusions, such as chlorite flakes and quartz grains. The presence of highly deformed thin wavy layers of apatite (up to a few hundreds of micrometres in thickness; Fig. 3C to E), which exhibit some kind of laminated textures and no remaining porosity (Fig. 3C), can be observed in several

samples. Deformed flattened rhombic shaped inclusions (Fig. 3D and E; feldspar relicts replaced by quartz?) are present in these layers/lenses. Besides apatite nodules, other nodules of the Middle Cambrian rocks are made of quartz grains, phyllites or deformed lenses of pyrrhotite. They are all set in a matrix of chlorite, muscovite, pyrrhotite and minor calcite (Fig. 3A to E). Deformation in the studied samples is also evidenced by pressure shadows, which are common around quartz or sulphide grains, and crenulation cleavage that locally develops in the shales (as described by Piessens & Sintubin, 1997). Pluri-micrometric monazite, xenotime and allanite assemblages are rather frequently found at the rim of the apatite nodules, in contact with sulphides (Fig. 3F), or as tiny grains in the nodules (Fig. 3E). Other REE-minerals (bastnaesite) are present as vein infillings in association with calcite. In the Middle Ordovician silty conglomerates that are predominantly made of quartz and chlorite (Fig. 3G), apatite nodules present an ellipsoidal/elongated shape (from 1.5 mm to a few millimetres long; Fig. 3G and H). They are homogeneous, without any remaining porosity, but are brecciated. The most striking feature of these nodules is the presence of spessartine porphyroblasts that are typically up to 200 μm in size (Fig. 3G and H).

Regarding their luminescence and Raman spectra, apatite nodules in Middle Cambrian and Middle Ordovician formations share many similarities. First, the bright green luminescence of apatite is dominant in these facies (Fig. 3B, D and H). The link between the CL colour and activation by a specific element can be deduced from cathodoluminescence spectra (Fig. 5A). The green shades are induced by Dy^{3+} (for the Middle Cambrian samples GH2743 and GH2952) and Mn^{2+} (particularly for the Middle Ordovician sample THY). The REE and Mn are elements that are typically responsible for the green CL of apatite (e.g. Waychunas, 2002; Baele *et al.*, 2019). A contribution of Sm^{3+} is also noted in the spectra, although it usually induces reddish shades (Waychunas, 2002). Another distinctive feature of the Middle Cambrian and Middle Ordovician apatite is the well-defined peaks in the Raman spectra. Complementary data relating to the photoluminescence are revealed by these spectra, when the Raman shift is converted back to the absolute emission wavelength (Fig. 5B) (Decrée *et al.*, 2016, 2020b). Beside the peaks that are typical of the vibrational mode of the PO_4^{3-} in apatite (ν1 at around 963 cm^{-1}, ν2 mode at *ca* 430 cm^{-1}, ν4 centred on *ca* 590 cm^{-1}; Penel *et al.*, 1997; Antonakos *et al.*, 2007), there are other well-defined peaks that are mostly related to MREE-induced fluorescence (Sm^{3+}, Eu^{3+} and Dy^{3+}; Kempe & Götze, 2002) and to the presence/abundance of these elements in the apatite (Fig. 5B). Overall, there is a good consistency between the CL and Raman spectra, with both the Cambrian and Ordovician apatites exhibiting clear REE emission lines while other apatites show a broadband emission centred on 575 to 580 nm interpreted as Mn^{2+}-activated. In Ordovician apatite, REE emission lines are weaker than in the Cambrian apatite and overwhelmed by a strong Mn^{2+} luminescence. Although visible, these REE lines cannot be fully resolved in the CL spectrum because of the poor spectral resolution of the CL spectrometer.

Late Cretaceous phosphorites

The Maastrichtian phosphatic calcarenite is mostly composed of coarse silt-sized and very fine sand-sized brownish phosphatic grains/peloids, embedded in a chalky matrix that also contains quartz, calcite and glauconite grains (Fig. 4A and B). The chalk matrix is rich in foraminifera bioclasts (Fig. 4B), although coccoliths are also present. All of these particles are loosely packed together due to the scarcity of calcitic cement. Consequently, much of the porosity is preserved. The phosphatic peloids form the exceeding majority of the phosphatic grains followed by marginal bones and teeth fragments. They present various degrees of phosphatization and they are commonly truncated/brecciated. Some of them are deposited in sediment that experienced additional phosphatization stages. These features have been carefully described by Jacquemin (2020). In the La Malogne quarry (at the edge of the Mons Basin), the conglomeratic beds are rich in rounded, intensely and homogeneously phosphatized pebbles embedded in a moderately phosphatized matrix that is still rich in calcite (Fig. 4C and D; sample LM4). Some of the phosphate pebbles are heavily perforated by multiple microborings of 1 mm or less in diameter filled mainly by carbonate-rich materials. Sand-sized grains of glauconite can be found in these pebbles, as well as phosphatic granules formed earlier on. The 'phosphatic sands' filling karstic pockets resulting from the dissolution of the host rock at La Malogne (sample LM3) present very distinctive features. Only little of the original carbonate matrix has been preserved in some highly phosphatized grains.

The CL emission of the phosphatic grains is overwhelmed by the strong yellow-brown

emission from the calcite cement and inclusions (Fig. 5A). A few grains show a faint, but distinct bluish-violet CL colour, which suggests REE activation. However, REE lines are difficult to observe in CL spectra mainly because of the strong Mn^{2+} emission of calcite. REE activation in Maastrichtian apatite can be better evidenced by spectral imaging of the Nd^{3+} emission (Fig. 5D) around 875 nm, which suppresses the intense Mn^{2+} luminescence from calcite. This technique also reveals phosphatic grains that were not visible at all using colour CL imaging because of their weak CL emission. Phosphatic grains with very different intensity of the Nd emission coexist, which suggests that these grains were reworked from sources with different phosphatization and/or REE enrichment stages. The Raman spectra are characterized by a broadband fluorescence, without any peak (Fig. 5C).

Cenozoic apatite nodules

The apatite nodules in Cenozoic P-rich rocks are made of quartz, glauconite and K-feldspar subangular to sub-rounded reworked grains embedded in an apatite matrix (Fig. 4E to G). In the Early Eocene nodules, the size of the silicate grains (mostly non-luminescent glauconite and violet-luminescent quartz; Fig. 4E) is typically about a few tens of microns. By contrast, in the Lower Oligocene and Middle Miocene nodules and concretions, the size of the grains ranges commonly between 200 μm and >1 mm in size (Fig. 4F and G). Quartz is dominant over glauconite (which has a dull blue-violet luminescence) and K-feldspar (bright blue under CL) as inclusions.

Apatite's luminescence is greenish-brown in these Cenozoic apatite nodules (Fig. 4B, D, F, H and J). It is likely due to activation by Mn^{2+}, as suggested from cathodoluminescence spectra (Fig. 5A). As for the Late Cretaceous apatite, the Raman spectra of Cenozoic apatite are dominated by a broadband emission (Fig. 5C).

Chemistry of apatite

Apatite from the studied phosphate samples shows a large range of CaO contents (48.27 to 55.14 wt.%). It is also characterized by two different ranges of P_2O_5 concentrations. Apatite from the Middle Cambrian and Middle Ordovician formations shows P_2O_5 contents that vary between 38.91 wt.% and 41.80 wt.%, whereas Late Cretaceous and Cenozoic apatite exhibits lower phosphate contents, between 29.96 wt.% and 32.83 wt.% P_2O_5. The latter correspond to a deficit at the P site (Table S2), which is easily explained by substituting CO_3^{2-} at this site in francolite. Apart from the Lower Palaeozoic apatite (that contains from 2.68 to 3.77 wt.% F), the analyses indicate an excess in fluorine in the mineral structure (with contents between 3.42 and 4.57 wt.% F). Chlorine concentration is usually below the detection limit; SO_3 content is substantial only in the youngest apatite (Late Cretaceous–Middle Miocene), ranging between 1.28 wt.% and 1.99 wt.%. SiO_2 concentrations are low in apatite from the Middle Cambrian, Middle Ordovician and Late Cretaceous rocks (up to 0.30 wt.%), whereas they are higher in the Cenozoic apatite (from 1.12 to 3.09 wt.% SiO_2). FeO and Na_2O contents are moderate in most apatites (below 1.09 wt.% and 1.21 wt.%, respectively), though FeO content reaches 3.95 wt.% in the Middle Ordovician sample. MnO contents are low (<0.19 wt.%) but reaches 3.29 wt.% in Middle Miocene apatite. Low to moderate contents are also observed for SrO (from 0.07 to 0.37 wt.%) and MgO (up to 0.25 wt.%). BaO content is above the detection limit in only two samples (0.05 wt.% and 0.06 wt.% BaO).

The post-Archean Australian shales (PAAS; Condie, 1993) normalized REE patterns of apatite from Middle Cambrian rocks (Fig. 6A) display a bell-shaped pattern, with $(La/Sm)_N$ and $(Gd/Yb)_N$ ratios varying from 0.07 to 0.21 and from 4.4 to 21, respectively (see Table S3). The range of REE contents is lower in highly deformed lenses/layers (ΣREE = 677 and 886) than in ellipsoidal nodules (968 < ΣREE < 1706). Europium anomaly is different in these two concretion types, being positive in deformed lenses/layers (Eu/Eu* = 2.2) and negative in ellipsoidal nodules (Eu/Eu* = 0.63 to 0.71), whereas no Ce anomaly is noticeable in either type (Fig. 6A). Rare earth element content of apatite from the Middle Ordovician formation is higher than in Middle Cambrian apatite (ΣREE = 2408 ppm and 3890 ppm), with an enrichment in LREE (La_N/Yb_N = 6.4 and 8.2), a slightly negative Ce anomaly (Ce/Ce* = 0.94 and 0.95) and a distinctive positive Eu anomaly (Eu/Eu* ≅ 2.2) (Fig. 6A).

Late Cretaceous apatite is either depleted in REE compared to the PAAS (ΣREE = 20 ppm and 21 ppm) when forming phosphatic pebbles in the conglomerate, or slightly to moderately enriched in REE (170 < ΣREE < 466 ppm) when apatite is present as grains/cement in the phosphatic calcarenite (Fig. 6B). The latter is characterized by a slight enrichment in LREE (La_N/Yb_N between 1.1 and 1.4), whereas apatite from phosphatic pebbles

Fig. 2. Selected macrophotographs and field pictures of phosphate-rich samples from Belgium. (A) Apatite as nodules and highly deformed lenses/layers (highlighted by white arrows) in intercalated slates and quartzites. Middle Cambrian formations (sample GH2952). (B) Brecciated phosphate-rich siltite bed (sample GH2946, upper figure) and porphyroclast of slaty quartzite containing ellipsoidal apatite nodules (a few nodules are indicated by white arrows, sample GH2743, lower figure) of the Middle Cambrian formations. (C) Apatite nodules (black or dark grey, indicated by the white arrows) in a Middle Ordovician conglomerate bed (silty matrix; sample THY1). (D) Phosphatic calcarenite with high content of brownish phosphatic particles (mainly peloids); high grade section of the Late Cretaceous Ciply Phosphatic Chalk Formation (sample Hb79.06). (E) Conglomeratic bed/lens (Late Cretaceous in age) with high concentration of phosphatic grains of the La Malogne underground quarry. No stratification is present in the phosphatic chalk enclosing this conglomeratic bed. Hammer for scale is 33 cm long. (F) Lower Oligocene apatite nodules in the Boom Clay Formation (internal mould of a gastropod; sample STN1). (G) Early Eocene (sample MO, upper figure) and Middle Miocene (samples BERCH1, lower figure) apatite nodules.

is somewhat enriched in HREE (La_N/Yb_N = 0.94). A distinctive negative Ce anomaly (Ce/Ce* = 0.18 to 0.28) is systematically present. No significant Eu anomaly is reported (Eu/Eu* = 094 to 1.1, Eu/Eu* = 0.81 for sample LM4-2).

Rare earth element patterns of Early Eocene apatite are somewhat similar to those of the Late Cretaceous apatite, with a slight enrichment in REE (426 < ΣREE < 88 ppm) and a slight depletion in LREE ($La_N/Yb_N \cong 0.69$ to 0.81). A major discrepancy is the lack of Ce anomaly (0.89 < Ce/Ce* < 1.1) in Early Eocene apatite compared to Late Cretaceous apatite. Lower Oligocene apatite is depleted in REE (ΣREE = 37 ppm and 72 ppm). The corresponding REE patterns are flat or somewhat concave downward, with a slight enrichment in LREE [$(La/Sm)_N$ = 29]. Only slight negative Ce anomalies are noted (Ce/Ce* = 0.73 and 0.87). The Middle Miocene apatite is neither significantly enriched nor depleted compared to the PAAS (ΣREE = 369 ppm and 370 ppm). The patterns are slightly concave-downward shaped [$(La/Sm)_N \cong 0.60$; $(Gd/Yb)_N \cong 2.1$], but not fractionated otherwise [$(La/Yb)_N$ = 1.2 to 1.3]. These patterns are also characterized by a positive Ce anomaly (Ce/Ce* ≅ 1.6), without any significant Eu anomaly (Eu/Eu* = 1.1).

Oxygen and strontium isotopic compositions of apatite

The O isotopic compositions of apatite are given in Table S4 ($1\sigma < 0.2$) and shown in Fig. 7. The

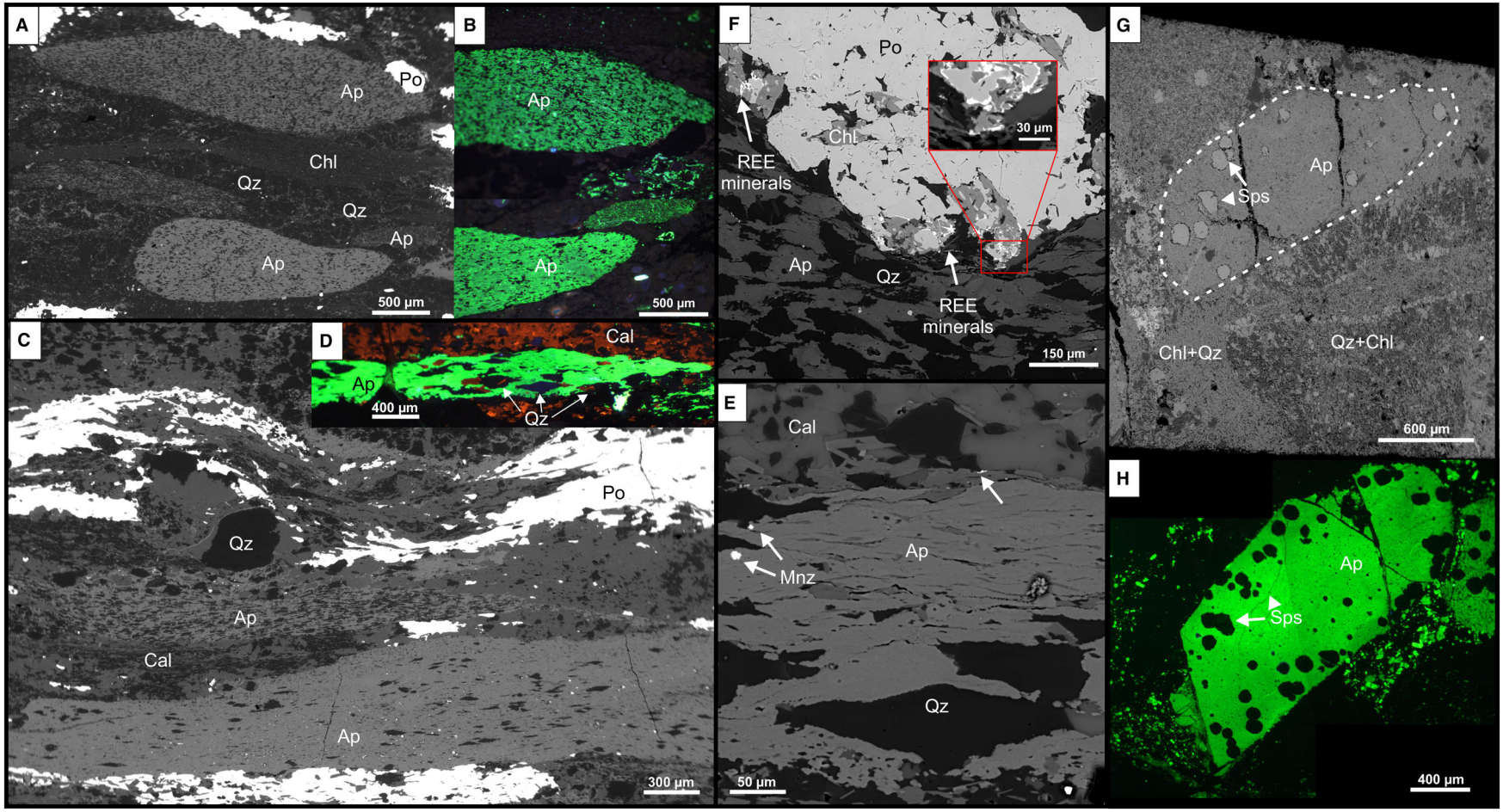

Fig. 3. Middle Cambrian (A) to (F) and Middle Ordovician phosphorite (G) and (H) from Belgium. Backscattered electron (A), (C), (E) to (G), and cathodoluminescence (B), (D) and (H) micrographs. (A) and (B) Apatite nodules in a matrix made of quartz and chlorite and comprising pyrrhotite lenses (sample GH2743). Green-luminescent apatite nodules contain quartz grains and chlorite flakes in various proportions. (C) and (D) Green-luminescent apatite forming highly-deformed thin lenses/layers in a silty cement comprising calcite and pyrrhotite nodules (sample GH2952). (E) Monazite grains (indicated by white arrows) in deformed apatite from one of the deformed lens/layer. Note the flattening of apatite and inclusions in the nodule (sample GH2952). (F) Rare earth element (REE) minerals deposited formed in contact with apatite (deformed nodule) and pyrrhotite. The inset shows a close-up on a zone of interest, where the brightest mineral assemblages are made of allanite, monazite and xenotime (sample GH2952). (G) and (H) Green-luminescent apatite nodule containing spessartine porphyroblasts in a conglomeratic bed mostly made of chlorite and quartz (sample THY1). A, apatite; Cal, calcite; Glt, glauconite; Kfs, K-feldspar; Mnz, monazite; Po, pyrrhotite; Qz, quartz; Sps, spessartine.

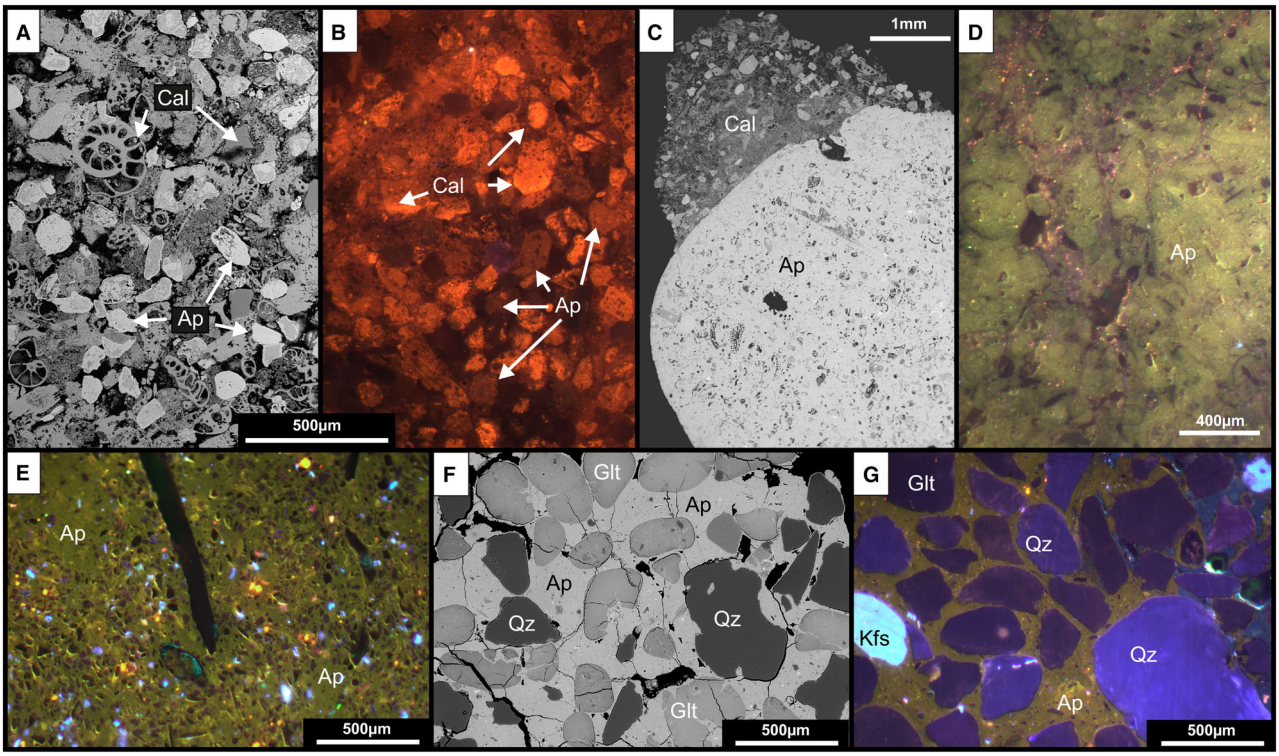

Fig. 4. Late Cretaceous phosphorites of the Mons Basin (A) to (D), Early Eocene apatite nodule (E), Lower Oligocene apatite nodules (F) and Middle Miocene apatite nodules (G) from Belgium. Backscattered electron (A), (C) and (F) and cathodoluminescence (B), (D), (E) and (G) micrographs. (A) and (B) Brown-luminescent phosphatic grains in the Ciply Phosphatic Chalk Formation, which consists of numerous orange-luminescent calcitic debris, bioclasts such as foraminifera, coccoliths and other shells (sample Hb79.06). (C) and (D) Phosphatic pebble enclosed in calcitic – and partly phosphatized – cement from a conglomeratic bed of the La Malogne underground quarry. Apatite exhibits a greenish-brown luminescence (sample LM4). (E) Apatite nodule in which small quartz and glauconite grains are cemented by greenish-luminescent apatite (sample MO). (F) and (G). Quartz, K-feldspar and glauconite grains cemented by greenish-brown luminescent apatite [sample STN1 for (F) and BERCH2 for (G)]. A, apatite; Cal, calcite; Glt, glauconite; Kfs, K-feldspar; Qz, quartz.

$\delta^{18}O$ values can be different from one sample to another in a formation of the same age, and even intra-nodule variation can be considerable. In the Middle Cambrian phosphorites, apatite from the most deformed phosphate layers/lenses (sample GH2952) shows $\delta^{18}O$ values between 7.3‰ and 9.4‰, whereas these values range from 10.9 to 11.5‰ for apatite from ellipsoidal nodules that are hosted in the sample that appears the least deformed (apatite nodules embedded in lithoclasts of siltite; sample GH2743). In the Middle Ordovician rocks, the $\delta^{18}O$ ratios of apatite vary from 7.6 to 9.6‰. The $\delta^{18}O$ values of apatite from the Late Cretaceous phosphatic calcarenite and conglomerates are heavier and fall within the range 18.5 to 22.3‰. The O isotope composition of apatite in Early Eocene formations ranges between 18.6‰ and 20.5‰, whereas the $\delta^{18}O$ values of apatite in Lower Oligocene and Middle Miocene formations vary from 20.5 to 24.1‰ and from 21.6 to 23.6‰, respectively.

The Sr isotope compositions of the studied apatites are presented in Table S4 and Fig. 8. The initial isotopic ratios have been calculated based on their emplacement age (see Table S4). As for the O isotope composition, the variations in initial $^{87}Sr/^{86}Sr$ ratios ($Sr_{(i)}$) can be significant in a single formation or even within a single nodule. The $Sr_{(i)}$ of apatite from Middle Cambrian formations varies from 0.7052 ($1\sigma = 0.0715$) to 0.7538 ($1\sigma = 0.0362$). The low precision of the measured Sr isotopic ratios for these samples is linked to their high Rb content, and the errors of the ^{87}Rb correction on ^{87}Sr. The initial $^{87}Sr/^{86}Sr$ ratios of the Middle Ordovician rocks are similar, ranging from 0.7186 ($1\sigma = 0.0011$) to 0.7234 ($1\sigma = 0.0009$). Apatite

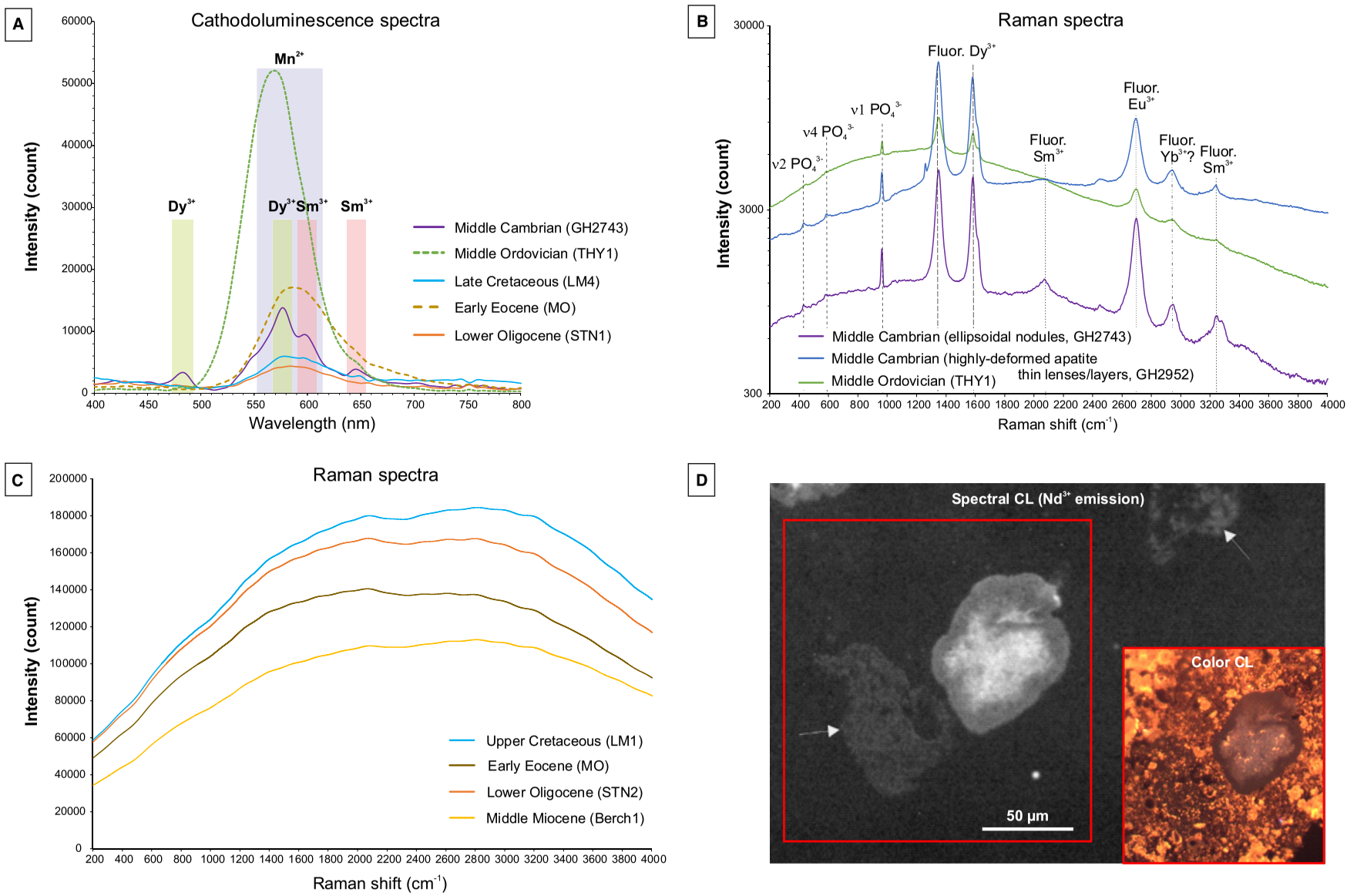

Fig. 5. Representative spectra using cathodoluminescence (A) and Raman spectroscopy (B) and (C), and cathodoluminescence micrograph showing the emission of Nd^{3+} (D) of apatite from various P-rich rocks from Belgium. The use of the Nd filter highlighting the CL emission of Nd^{3+} (D) reveals the presence of peloids (arrows) characterized by various intensity of phosphatization, which is hardly discernible in simple CL images [inset in (D)] (modified after Jacquemin (2020)).

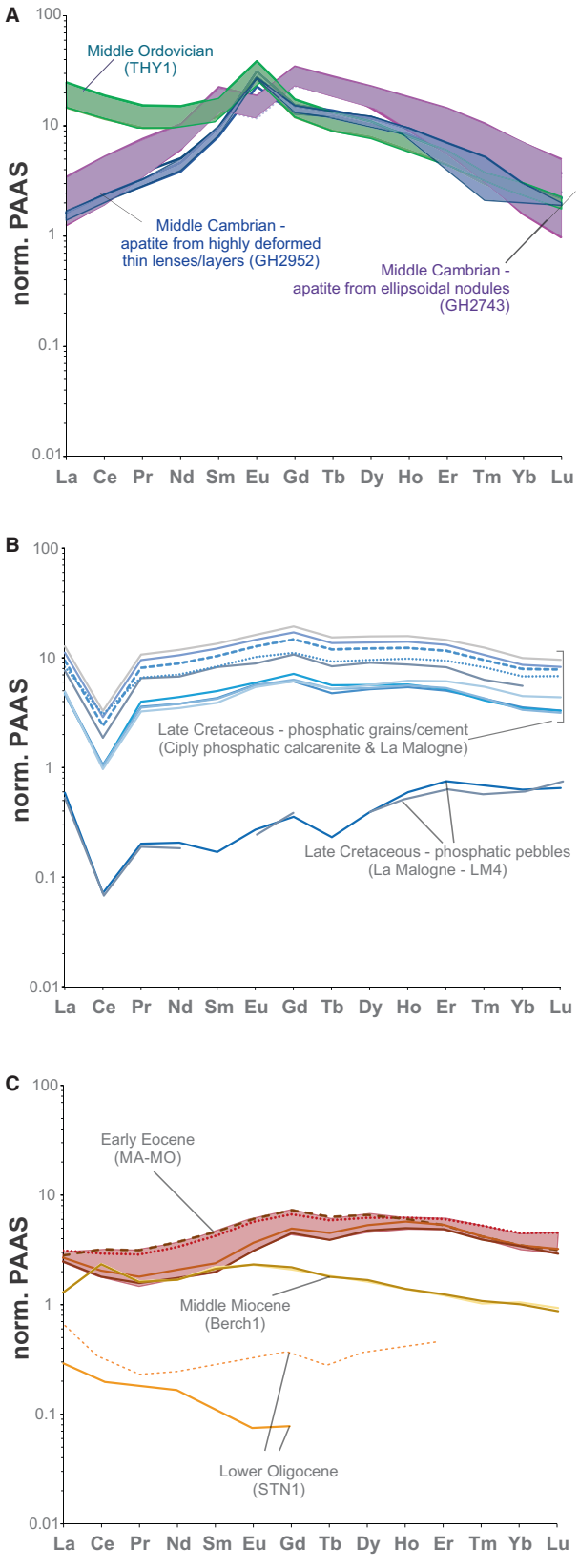

Fig. 6. Rare earth element (REE) patterns of apatite in the different P-rich rocks investigated [laser ablation – inductively coupled plasma – mass spectrometry (LA-ICP-MS) analyses]. REE patterns are normalized to the Post Archean Australian Shales (PAAS; Condie, 1993).

from the Late Cretaceous phosphatic chalk is less radiogenic, with values between 0.7067 ($1\sigma = 0.0005$) and 0.7087 ($1\sigma = 0.0013$). The $^{87}Sr/^{86}Sr$ ratios of apatite from one of the Early Eocene samples (sample MA) range between 0.7093 ($1\sigma = 0.0007$) and 0.7097 ($1\sigma = 0.0009$), whereas the $Sr_{(i)}$ of apatite hosted by the other sample (sample MO) fluctuates within a wide range from 0.7071 ($1\sigma = 0.0008$) and 0.7129 ($1\sigma = 0.0037$). The $Sr_{(i)}$ of apatite from Lower Oligocene formations varies from 0.7049 to 0.7077 (in one sample; STN2). Apatite from the Middle Miocene formations yielded initial $^{87}Sr/^{86}Sr$ ratios in the same compositional range [$Sr_{(i)}$ from 0.7088 ($1\sigma = 0.0008$) to 0.7126 ($1\sigma = 0.0032$)].

DISCUSSION

Mineralogical and petrological investigation of sedimentary P-rich rocks from the Middle Cambrian to the Middle Miocene makes it possible to discriminate several apatite types with distinct morphotypes, mineralogical characteristics (Raman spectra, CL) and geochemical attributes. This information provides interesting insights into specific phosphogenesis, diagenesis and metamorphism affecting apatite.

Insights into phosphogenesis at a regional scale

Textural and mineralogical features evidence various depositional settings and different ways and intensities the apatite concretions were affected by post-depositional alteration, including metamorphism.

Middle Cambrian and Middle Ordovician apatite nodules

The Lower Palaeozoic apatite differs from the younger apatite by: (i) its bright green cathodoluminescence; (ii) its Raman spectra that exhibit

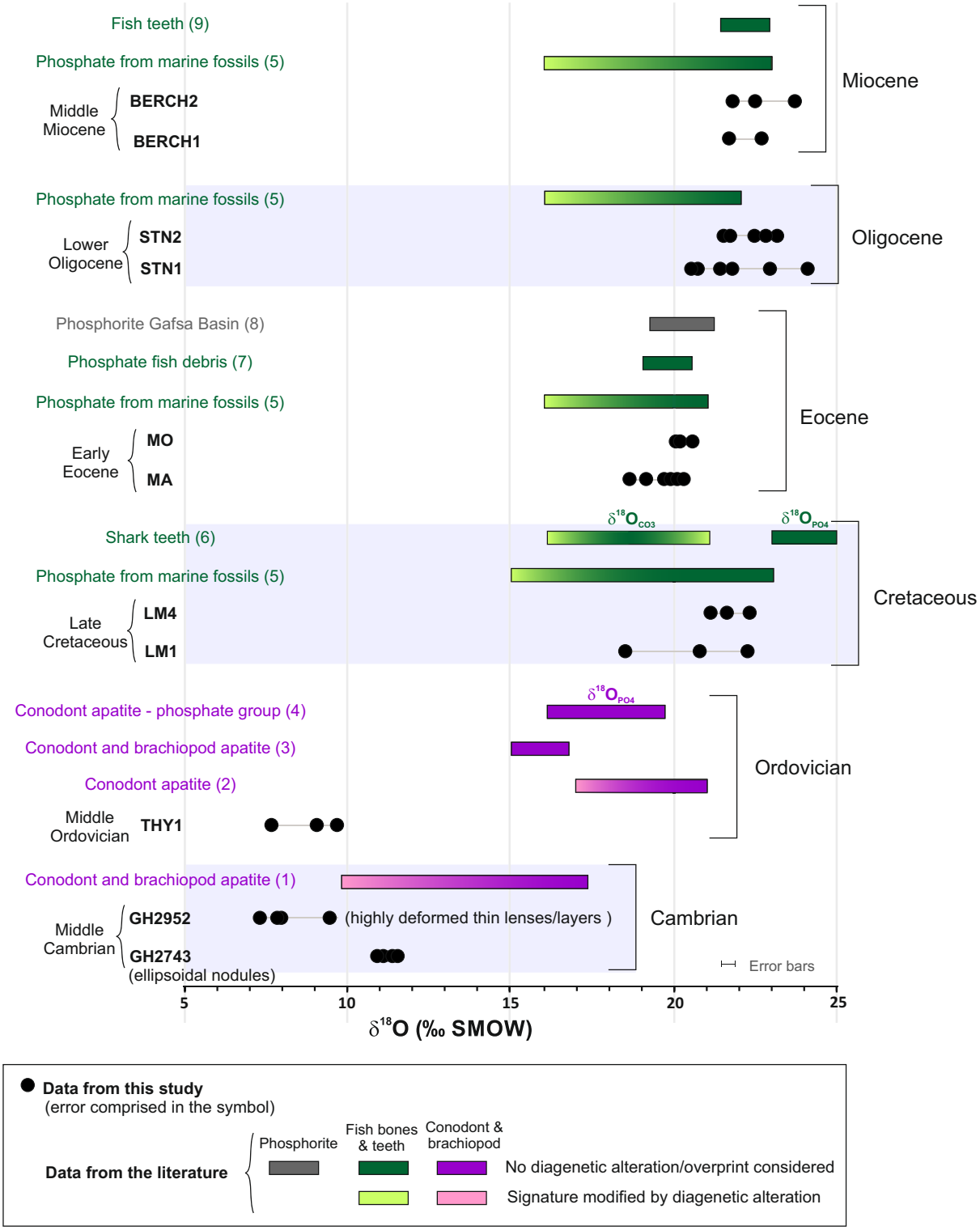

Fig. 7. *In situ* $\delta^{18}O$ for apatite hosted in the different P-rich rocks from Belgium; data from the literature are given for comparison. The references are indicated between brackets, as follows: (1) Wotte *et al.* (2019); (2) Elrick *et al.* (2011); (3) Bassett *et al.* (2007); (4) Quinton *et al.* (2017); (5) Longinelli *et al.* (2002); (6) Kocsis *et al.* (2009a); (7) Lécuyer *et al.* (1993); (8) Ounis *et al.* (2008); (9) Kocsis *et al.* (2009b).

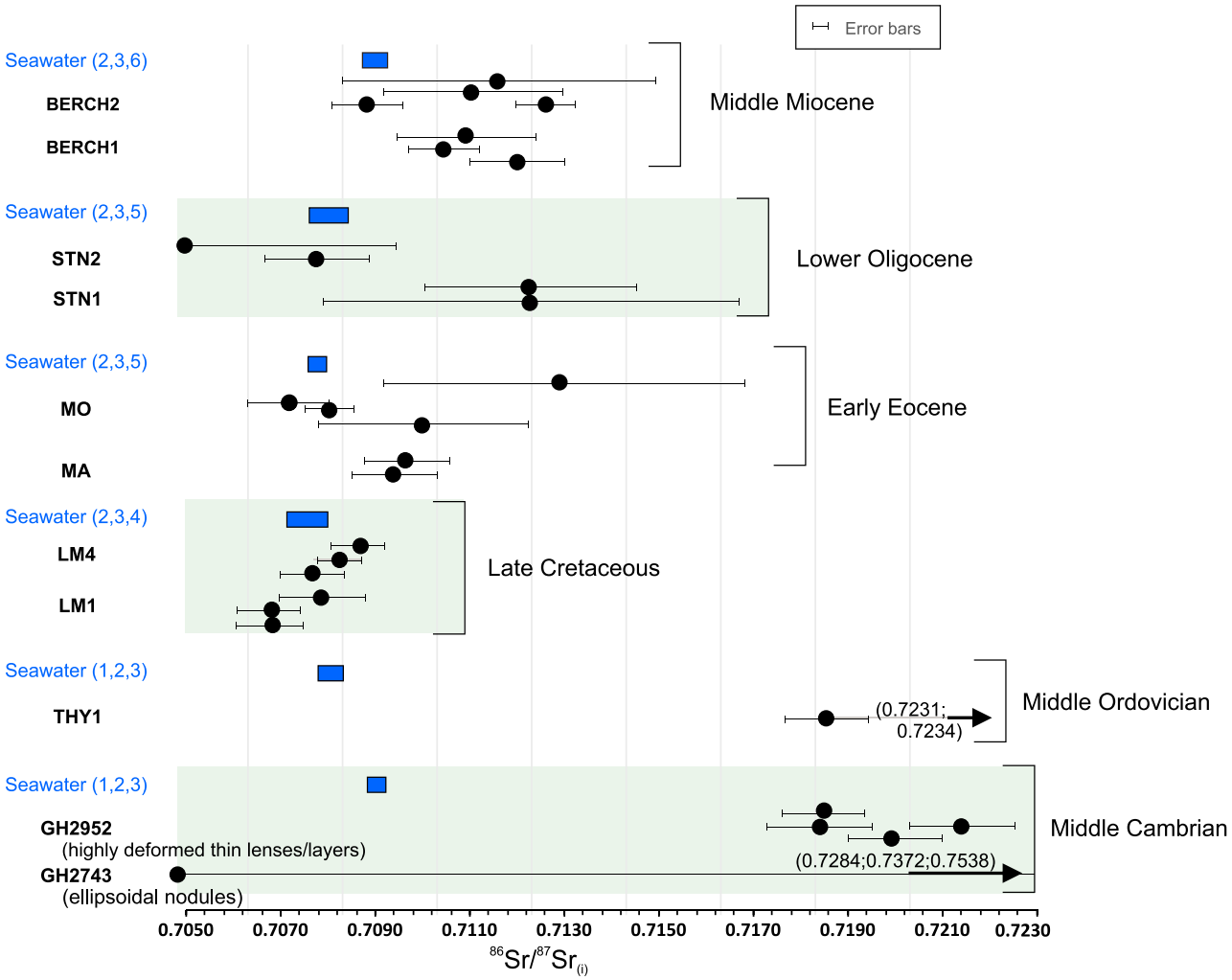

Fig. 8. *In situ* $^{87}Sr/^{86}Sr_{(i)}$ (initial isotopic ratios recalculated based on their formation age) for apatite hosted in the P-rich rock investigated. Data from the literature (seawater Sr isotope composition) are given for comparison. The references are indicated between brackets, as follows: (1) Denison *et al.* (1998); (2) Hannisdal & Peters (2011); (3) Veizer *et al.* (1999); (4) Burke *et al.* (1982); (5) Koepnick *et al.* (1985); and (6) Jarvis (1994).

well-defined Raman peaks and suggest a well-organized crystallographic structure of apatite (e.g. Tuschel, 2017); and (iii) its composition, which proves to be fluorapatite (see EMPA analyses, Table S2). These characteristics testify to the transformation of the primary poorly-crystallized carbonate fluorapatite – which is primarily formed during phosphogenesis (e.g. McArthur, 1985; Trappe, 2001) – to a well-crystallized fluorapatite. It is known that compaction, deep-burial diagenesis and metamorphism alter the composition of primary carbonate fluorapatite towards a more stable fluorapatite (McArthur, 1985; McClellan & Van Kauwenbergh, 1991; Jarvis, 1994), which is dominant in all metamorphic facies compared to carbonate fluorapatite (Spear & Pyle, 2002).

The impact of metamorphism is obvious in the rocks considered. The Middle Cambrian P-rich rocks come from the southern part of the Stavelot Massif, which has undergone two metamorphic events. These rocks are deformed, with a crenulation cleavage in some of the shaliest samples, and locally brecciated and reworked, up to form sub-rounded porphyroclasts embedded in more shaly layers (Fig. 2B). Apatite (and sulphide) concretions in these P-rich rocks are commonly deformed and recrystallized (Fig. 3). The intensity of the deformation and recrystallization of apatite likely depends on the dominant

lithology. For instance, apatite nodules that are transferred to the deeper part of the basin as inclusions in siltite lithoclasts (as illustrated in the lower part of Fig. 2B) would have been less exposed to the mechanical effects of burial metamorphism and experienced limited stretching and flattening (Fig. 3A and B). By contrast, highly elongated and flattened apatite lenses are observed in more shaly rocks (Figs 2A, 3C and 3D). Whether the apatite concretions are slightly or significantly deformed, newly formed REE-bearing minerals (monazite, xenotime and allanite) are commonly observed within the concretions or at their immediate vicinity. Besides, bastnaesite (REE-fluorocarbonate) occurs in fissures induced by the Variscan orogeny. This would attest for a mobilization and reprecipitation of REE during deformation (see *Further investigations about sources and post-depositional processes* section).

The investigated Middle Ordovician P-rich rocks are in a part of the Brabant Massif that is characterized by an epizonal metamorphic grade (Debacker *et al.*, 2002). The influence of the metamorphism in these samples is obvious. Spessartine porphyroblasts co-crystallized with apatite in nodules that are homogeneous and without any other inclusion or remaining porosity otherwise. This suggests an intense recrystallization of the primary carbonate fluorapatite, due to metamorphism reaching the grade corresponding to the formation of spessartine. The latter would form through the diffusion of Mn^{2+} in amorphous phosphate (de Magnée & Lambeau, 1965). The coeval recrystallization of apatite and formation of spessartine porphyroblasts through Mn diffusion is further supported by the strong bright green CL activation of apatite by Mn^{2+} (as shown in the CL spectrum; Fig. 5A). As suggested for the coticule of the Stavelot Massif (Schreyer *et al.*, 1992; Herbosch *et al.*, 2016), Mn^{2+} could originate from Mn-rich shales, and have migrated into turbiditic limy mud beds through diffusion during early diagenesis. Spessartine would then result from the reaction of aluminosilicate from a P-rich mud with Mn-carbonates in epizonal areas. Such Mn-rich mud should have existed in the Brabant Massif, since a few horizons enriched in spessartine have been described in the Upper Cambrian formations (Assise de Mousty; Michot, 1980).

Apart from the metamorphism, the Middle Cambrian and Middle Ordovician P-rich rocks are strongly reworked. The Middle Cambrian apatite nodules locally host inclusions that clearly do not originate from the host rock (for example, large quartz inclusions in apatite nodules, the latter being embedded in a carbonate-rich shaly matrix). This indicates that apatite nodules came from another depositional environment. The structureless, rounded to sub-rounded textures of apatite nodules (Fig. 3) further support the allochthonous character of the nodules and reinforce the idea of mechanical transport of the phosphatic material, at least over short distances. Therefore, these nodules can be regarded as phoslithoclasts (as defined by Trappe, 2001). In the Middle Cambrian of the Stavelot Massif, the conglomerate beds rich in phosphate nodules are thought to mark the base of a turbiditic sequence deposited in a deep pelitic environment, associated with hemipelagite (Michot, 1980; von Hoegen *et al.*, 1985; Herbosch *et al.*, 2016). Such turbidite basins flanking the Avalon Platform were inferred by Brasier (1980). The phosphate nodules would have been primarily formed on the inner shelf, in phyllitic or siliciclastic material, probably at the favour of the Lower–Middle Cambrian transgression. The latter is responsible for the remarkable phosphogenic Cambrian event in the Avalon and Baltic region (Brasier, 1980; Notholt & Brasier, 1986).

Although a dominantly allochthonous origin of the apatite nodule is inferred, the nature of the highly deformed apatite lenses/layers remains uncertain. The compaction of these layers is distinct, as emphasized by the presence of recrystallized inclusions presenting a flattened rhombic shape. Nevertheless, the roughly laminated structure could represent a phosphatic bindstone that formed once the turbidite was deposited, probably as a result from microbial mat phosphatization when the rock was not lithified yet (e.g. Krajewski *et al.*, 1994; Föllmi, 1996; Pufahl & Groat, 2017). Even if two different phosphatization periods – before and after turbidite deposition – could be considered, all of the Middle Cambrian apatite concretions largely share common mineralogical and geochemical features (see above and also *Lower Palaeozoic apatite nodules* and *Further investigations about sources and post-depositional processes* sections) and can be regarded as belonging to the same big phosphogenic event.

In the Middle Ordovician conglomerate of the Brabant Massif remains, the abundance of siltstone to sandstone clasts showing the same lithology than the host formations of the conglomerate, and the absence of sorting among these clasts argue for a proximal source for the source material of the clasts (de Magnée & Lambeau, 1965), which

would have been located to the north of the present position of the conglomerate (considering the slump transport directions; Debacker *et al.*, 2009). The source of the phosphatic nodules should originate from the same area, further north compared to the location of the conglomerates.

Late Cretaceous phosphorites and Cenozoic apatite nodules

By contrast with the Lower Palaeozoic apatite nodules, the Late Cretaceous and Cenozoic concretions show a greenish-brown luminescence (Fig. 4). This apatite also presents a carbonate fluorapatite composition, and a strong broadband fluorescence in the Raman spectra, which is likely related to the cryptocrystalline to microcrystalline texture of carbonate fluorapatite in sediments (e.g. Notholt, 1980; Trappe, 2001). The lack of spatial order in such material explains the absence of well-defined peaks in the Raman spectra (Tuschel, 2017). The shift of the CL colour due to Mn^{2+} activation from green in Lower Palaeozoic apatite to more brownish shades in Cenozoic apatite could be explained by a lower ordering and/or a different composition of apatite, especially a higher carbonate content (the CL colour of Late Cretaceous apatite is not observable because it is masked by the intense yellow-orange luminescence of calcite). Note that comparable shades of brownish CL colours were observed in apatite from Quaternary fossil bones and carbonate content in apatite was mentioned as a possible cause for the brownish CL colours that are strikingly different from the green CL colour in ancient Mn^{2+}-activated apatite (Baele *et al.*, 2011).

Although these concretions were apparently less exposed to late diagenesis/alteration, they can however record multiple phosphatization events and reworking/winnowing. For instance, in the conglomeratic bed of the Mons Basin, intensely phosphatized pebbles, which are also marked by the dissolution of calcite, are set in a moderately phosphatized cement. This testifies to the polyphase-character of the phosphatization. Other evidence can be found in the chalk series, where: (i) broken phosphatized grains are coated by a new generation of apatite; and (ii) grains showing significantly different intensity of phosphatization are found close to one another, as well-expressed using a Nd^{3+} emission filter in CL images (Fig. 5D). The latter reveals the presence of peloids (arrows) characterized by various intensity of phosphatization (emphasized by different colours), which is hardly discernible in simple CL images (inset in Fig. 5D; modified after Jacquemin, 2020). Most of the Cenozoic phosphorites possess a conglomeratic nature and include a variety of subrounded phosphate concretions (grains, nodules and pebbles) and fossils, like fish/shark teeth and bone fragments (Louwye *et al.*, 2010; Marquet & Herman, 2012). This would argue for reworking processes/winnowing of the sediments, probably through wave action during storms or sea-level variations, which are well-documented in these Cenozoic rocks (e.g. Balson, 1980; Louwye, 2005; De Man, 2006; Iserbyt & De Schutter, 2012).

Phosphogenesis from the Late Cretaceous onward was likely associated with a transgressive event and occurred in an epicontinental sea. It was also likely related to low oxygen bottom water and abundance of decaying organisms during the Eocene (Steurbaut, 1986; Iserbyt & De Schutter, 2012), Oligocene (Vandenberghe *et al.*, 2003; De Man, 2006) and Miocene (Louwye, 2005; Louwye *et al.*, 2010).

Phosphogenesis combined with intense reworking during major transgressive events are also invoked for the Middle Cambrian and Middle Ordovician P-rich rocks, as stated above. This would be the most efficient way to form large and economically interesting sedimentary phosphate deposits (Föllmi, 1996: Pufahl & Groat, 2017). This is clearly the case for the phosphatic calcarenite of the Mons Basin, which is one of the largest sedimentary phosphorite formations occurring in Europe, representing about 47 Mt of P_2O_5 (Robaszynski & Martin, 1988) with an estimate of *ca* 0.4 Mt of REE oxides (Jacquemin, 2020; Decrée *et al.*, 2022a,b).

Depositional conditions investigated using rare earth element signatures

Rare earth elements in apatite constitute a proxy of ancient pore water chemistry and, to some extent, of ancient seawater. This can be investigated through the examination of their REE patterns, trace element ratios and comparison of Ce, Pr and Eu anomalies (Fig. 9A, B, C and D) (e.g. McArthur & Walsh, 1984; Shields & Stille, 2001; Kidder *et al.*, 2003; Zhu *et al.*, 2014; Chen *et al.*, 2015; Álvaro *et al.*, 2016), which are helpful in deciphering depositional conditions and subsequent early diagenesis. The REE signatures of apatite are considered according to the age of phosphate deposit.

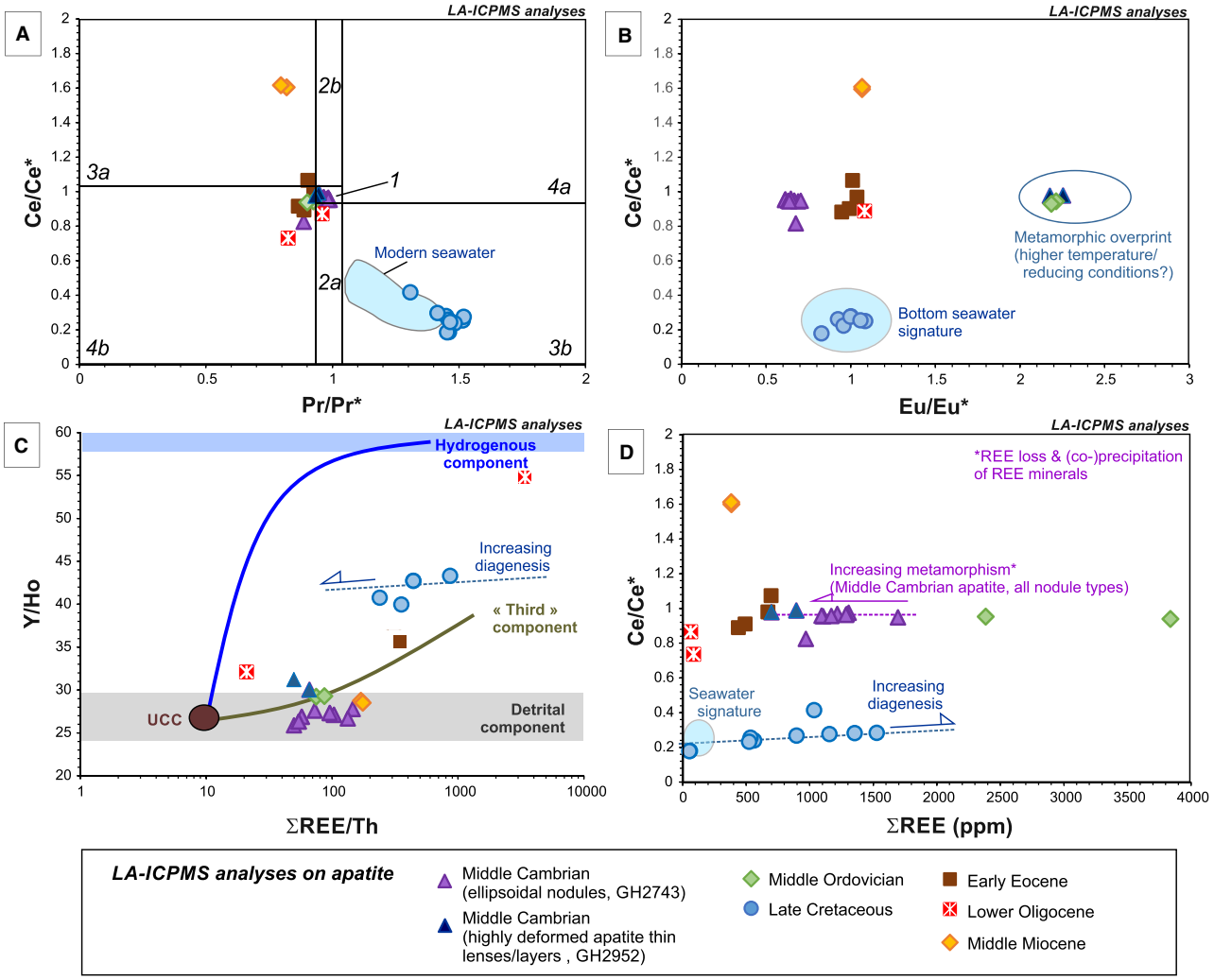

Fig. 9. (A) Distinction of the La and Ce anomalies of all the apatite laser ablation – inductively coupled plasma – mass spectrometry (LA-ICP-MS) analyses, based on the plot of Bau & Dulski (1996), where the fields are as follows: 1 – neither Ce nor La anomaly; 2a – positive La, no Ce anomaly; 2b – negative La, no Ce anomaly; 3a – positive Ce and negative La anomaly; 3b – negative Ce and positive La anomaly; 4a – negative Ce and negative La anomaly; 4b – positive Ce and positive La anomaly. Data of the modern seawater are reported for comparison purposes (Herwartz *et al.*, 2013; adapted from Nothdurft *et al.*, 2004). (B) to (D) Correlations for LA-ICP-MS analyses between Ce and Eu anomalies. Field for bottom seawater from Shields & Stille (2001) and Chen *et al.* (2009) (B), Y/Ho and ΣREE/Th ratios. Curves, fields and components taken from Chen *et al.* (2009) (C), and Ce anomalies and total REE contents. Field for bottom seawater from Shields & Stille (2001) (D).

Lower Palaeozoic apatite nodules

The Middle Cambrian apatite presents PAAS-normalized REE patterns that are characterized by an enrichment in MREE, a lack of significant Ce anomaly, and Eu anomalies that are negative for ellipsoidal nodules and positive for sub-continuous lenses/layers. The MREE enrichment is a common feature of phosphorites associated with Lower–Middle Palaeozoic shales (e.g. Jarvis, 1994; Shields & Stille, 2001; Emsbo *et al.*, 2015; Álvaro *et al.*, 2016). It is related to the formation of apatite nodules in sediments enriched in Fe-oxyhydroxide and organic matter (e.g. Elderfield *et al.*, 1990; Kidder *et al.*, 2003). The MREE adsorbed onto these phases are transferred to the pore water during changes of redox conditions and subsequent breakdown of these phases (e.g. Jarvis, 1994; Chen *et al.*, 2015; Álvaro *et al.*, 2016). As suggested by Brasier (1980), dark Middle Cambrian sediments associated with

phosphorites on the marginal basins of the Avalon platform, which is the setting of the Lower Palaeozoic Belgian phosphorites, argue for euxinic conditions. Besides, it is known that the MREE are preferentially removed from solution when phosphates and REE compounds are co-precipitated (Byrne *et al.*, 1996). The lack of significant Ce anomalies in the REE patterns (Fig. 6A) suggests that the release of Ce from the Fe-oxyhydroxides occurred in anoxic water, preventing Ce^{3+} from being oxidized into insoluble Ce^{4+} and then adsorbed onto/co-precipitated with oxyhydroxides (e.g. Chen *et al.*, 2015; Álvaro *et al.*, 2016; Gao *et al.*, 2018). Regarding the negative Eu/Eu^*_{PAAS} (from 0.63 to 0.72) observed in the less deformed ellipsoidal apatite nodules, it is commonly ascribed to an Eu-depleted source (e.g. Elderfield & Greaves, 1982; McArthur & Walsh, 1984; Shields & Stille, 2001; Kidder *et al.*, 2003) and interaction with low temperature solutions. The latter are typically characterized by negative Eu anomalies in the absence of chloride in the fluid (e.g. Bach & Irber, 1998; Shibata *et al.*, 2006).

In contrast, apatite from the lenses/layers that are believed to be impacted by a stronger metamorphic overprint is characterized by distinct positive Eu* (from 2.2 to 2.5). The latter is commonly explained by a higher REE input from hydrothermal solutions (Bau & Dulski, 1999). Bivalent europium (Eu^{2+}) that is dominant in reducing and slightly acidic solutions with temperature exceeding 200°C would preferentially partition into the dissolved phase relative to the trivalent REE, explaining the development of a positive Eu anomaly for apatite formed from these fluids (e.g. Bau *et al.*, 2010). A positive Eu anomaly can also develop in a closed reducing system, as the result of addition of Eu^{2+} (originating ultimately from the host rock) to the Eu^{3+} initially present in apatite structure (MacRae *et al.*, 1992; Kidder *et al.*, 2003). The slightly negative Eu anomalies reported in the reducing sediments of the Grand Halleux borehole (Burnotte *et al.*, 1989) could argue for this hypothesis.

The main differences in terms of geochemistry between ellipsoidal nodules and highly deformed layers/lenses (Eu anomalies and behaviour in the Ce/Ce* versus ΣREE diagram; Fig. 9B and D) are likely explained by an increasing effect of the deformation. It is recognized that the REE budget in apatite increases with progressive metamorphism (Henrichs *et al.*, 2019). Nevertheless, slight discrepancies regarding apatite chemistry are common in this kind of system, due to small-scale geochemical variations – notably regarding the redox conditions and element abundance – in pore water (Bau & Dulski, 1999; Shields & Stille, 2001; Kidder *et al.*, 2003). Considering that the most deformed lenses could be bindstone, one could also consider a different REE uptake due to microbial activity for the latter. However, studies show that there is no 'bacterial pumping' of REE from the pore water, as it is for P (Schulz & Schulz, 2005; Lumiste *et al.*, 2019).

By contrast with the Middle Cambrian phosphate nodules and lenses, the Middle Ordovician apatite is characterized by an enrichment in LREE. Although the latter is frequently encountered in magmatic alkaline contexts (e.g. Belousova *et al.*, 2002; Chakhmouradian *et al.*, 2017), it is less common in apatite forming sedimentary phosphorites. Here, the enrichment in LREE could be explained by the redistribution of REE during metamorphism and the preferential uptake of HREE by garnet (e.g. Grauch, 1989), which is overall coeval with apatite (cf. *Middle Cambrian and Middle Ordovician apatite nodules* section) and competes for the same REE reservoir (i.e. REE from the primary apatite with a possible REE contribution from metamorphic fluids). As for Middle Cambrian apatite, the presence of a positive Eu anomaly in the REE pattern (Eu/Eu* = 2.2) would highlight the contribution from a hydrothermal fluid (Bau *et al.*, 2010; see discussion above) and/or indicate highly reducing conditions (e.g. Kidder *et al.*, 2003).

Late Cretaceous phosphorites

The shape of the REE patterns of apatite from the Late Cretaceous phosphatic calcarenite is commonly observed among sedimentary phosphorites and shares similarities with the signature of open ocean seawater (e.g. McArthur & Walsh, 1984; Shields & Stille, 2001; Lécuyer *et al.*, 2004; Emsbo *et al.*, 2015; see also Fig. 9A and B for comparison of Ce, Pr and Eu anomalies). These patterns are even closer to the signature of pore water at the bottom seawater–sediment interface, which is supposed to experience suboxic conditions (Chen *et al.*, 2015). This is consistent with the hypothesis proposed by Jarvis (1992) that mineralization is dominantly a post-oxic process, with alternating/mixed redox conditions. The preservation of a prominent true negative Ce anomaly (Fig. 9A) demonstrates that oxygenated seawater has influenced the sediments where apatite formed to some extent (e.g. McArthur & Walsh, 1984; Ye *et al.*, 2020). At a

larger scale, the involvement of oxygenated and P-rich waters is invoked to explain the genesis of the Cretaceous phosphatic chalk on the north-eastern margins of the Anglo-Paris Basin (Jarvis, 1992; Jacquemin, 2020). A major difference between apatite from the Mons Basin and apatite from seawater and other phosphorites of the same age (even those occurring in the adjacent Paris Basin; Jarvis, 1994) is the lack of HREE enrichment in the former. Since the HREE-enriched patterns tend to develop whenever REE distributions are dominated by seawater (Chen *et al.*, 2015), this suggests that other sources are involved. According to Shields & Webb (2004), HREE depletion and other unseawater-like REE patterns in ancient phosphorites are likely to be related to post-depositional processes. Further discussion is provided below (see *Further investigations about sources and post-depositional processes* section).

Compared to apatite from the phosphatic calcarenite, apatite forming the pebbles in the conglomerates on the edge of the basin are significantly depleted in REE (although the depletion in HREE is less pronounced). These pebbles are also more intensely phosphatized (with a brighter CL) than the apatite concretions in the phosphatic calcarenite. These pebbles likely represent a slightly earlier stage of phosphatization, the product of which was reworked in deeper parts of the basin (Jarvis, 1992; Jacquemin, 2020). These pebbles would keep a more pristine REE signature, closer to the Cretaceous seawater, with low REE contents (cf. Shields & Stille, 2001). The enrichment in (L)REE would have been limited due to reworking and their transport a long way from their primary depositional/diagenetic environment.

Cenozoic apatite nodules

The Cenozoic apatite is characterized by an overall flat, shale-like pattern that can be slightly enriched or depleted in REE. Apatite from the Early Eocene and Middle Miocene phosphorites shows resemblance with apatite of the same age described by Shields & Stille (2001) and Ounis *et al.* (2008). This kind of pattern is thought to reflect detrital influence (e.g. Flicoteaux & Trompette, 1998; Kidder *et al.*, 2003), which is likely considering the high SiO_2 content of the Cenozoic apatite (from 1.12 to 3.09 wt.% SiO_2). The flat-distribution pattern without Ce anomaly is commonly assigned to their deposition in oxic to suboxic zone during early diagenesis (Chen *et al.*, 2015). Benthic fauna associated with these phosphates suggest that the sea bed was oxic (Balson, 1980). By contrast, the positive Ce anomaly observed for the Middle Miocene apatite would relate near-surface reducing near-shore/coastal sediments (e.g. Sholkovitz *et al.*, 1989).

Slight LREE/MREE depletion (for Early Eocene and Lower Oligocene apatite, respectively) and MREE enrichment (for Middle Miocene apatite) are observed and likely relate to post-depositional alteration of apatite. Preferential removal of LREE and MREE would be induced by weathering (as described by McArthur & Walsh, 1984), whereas slight MREE enrichment of the Middle Miocene apatite would involve Fe-oxides and changes of redox conditions. The abundance of glauconite in the Middle Miocene P-rich rocks would confirm at least temporary reducing conditions and the presence of suboxic pore water at the sea bottom (Balson, 1980). These conditions commonly lead to a positive Ce anomaly and the breakdown of Fe-oxyhydroxide that releases phosphate into the system (e.g. Elderfield *et al.*, 1990; Kidder *et al.*, 2003; Pufahl & Grimm, 2003).

Further investigations about sources and post-depositional processes

It appears from the mineralogical and REE pattern study that the investigated apatite displays evidence of post-depositional processes. These can be further deciphered by a set of other geochemical parameters (i.e. ΣREE, ΣREE/Th and Y/Ho ratios), which also give clues about sources for apatite-forming elements in these systems (e.g. Chen *et al.*, 2015; Gao *et al.*, 2018; Fig. 9C and D).

Apatite from the Middle Cambrian, Middle Ordovician and Middle Miocene conglomerates plots in the 'detrital component' field of the Y/Ho versus ΣREE/Th diagram, suggesting that most of the REE originates from this reservoir. By contrast, the Late Cretaceous, Early Eocene and Lower Oligocene apatite is characterized by Y/Ho ratios that are intermediate between a hydrogenous and detrital component, highlighting a contribution from both reservoirs for the REE. The Lower Oligocene apatite plots close to the ideal hydrogenous–terrigenous trend in the Y/Ho versus ΣREE/Th diagrams (Fig. 9C). By opposition, the Late Cretaceous and Early Eocene apatite plots off this trend. This suggests an external addition of REE to the system that likely relates to the release of REE scavenged by Fe-oxyhydroxides (or other minerals) in pore water

and their subsequent incorporation into apatite during diagenesis (as proposed for other P-rich systems; e.g. Chen *et al.*, 2015; Gao *et al.*, 2018; Decrée *et al.*, 2022b). Such a 'third' component (i.e. chemically-modified pore water) could also be considered for the Middle Cambrian, Middle Ordovician and Middle Miocene apatite, which shifts from the Upper Continental Crust end-member, although still showing a detrital signature (Fig. 9C). Besides, the Late Cretaceous apatite defines an additional trend that could emphasize the diagenetic alteration of the samples (as described by Chen *et al.*, 2015), the lower ΣREE/Th values reflecting increasing alteration and the preferential diagenetic enrichment of Th relative to REEs (Chen *et al.*, 2015). The positive correlation between Ce/Ce* and the total REE content of apatite (Fig. 9D), also supports such post-depositional alteration, which typically tends to increase REE contents and reverses Ce depletion (McArthur & Walsh, 1984; Shields & Stille, 2001). In this diagram presenting Ce anomaly versus the total REE content (Fig. 9D), it also appears that the REE content of Middle Cambrian apatite decreases with increasing deformation (from the ellipsoidal nodules to the highly deformed lenses/layers). This would suggest that part of the REE is lost during dissolution and regrowth of apatite throughout progressive metamorphism. This loss is likely due to competition for REE with minerals like allanite, monazite and xenotime (as documented by Nutman, 2007), which may form at low-grade metamorphism (e.g. Harlov & Förster, 2003) and are found at the vicinity of (or even within) phosphate nodules/lenses (see Fig. 3E).

Contribution of the Sr and O isotope compositions to the understanding of phosphogenesis and later processes

It is accepted that the O and Sr isotopic compositions of ancient apatite represents the seawater isotopic compositions at the time (e.g. Jarvis, 1994; Martin & Haley, 2000; Kohn & Cerling, 2002; Longinelli *et al.*, 2002; Quinton *et al.*, 2017). Deviation from these values would thus help to constrain the post-depositional history of apatite and give clues about processes such as (burial) diagenesis, weathering or involvement of hydrothermal fluids (Jarvis, 1994; Trappe, 2001; Brand *et al.*, 2011; Drummond *et al.*, 2015; Pufahl & Groat, 2017).

The initial $^{87}Sr/^{86}Sr$ ratios of the studied apatite are commonly higher than the Sr isotope composition of the corresponding seawater (Fig. 8). This shift towards more radiogenic values is typical of weathering, diagenetic and metamorphic processes (McArthur *et al.*, 1986; McArthur & Herczeg, 1990). The highest $Sr_{(i)}$ are observed for the Middle Cambrian and Middle Ordovician apatite. In these cases, the values are likely related to metamorphism that led to partial recrystallization of apatite (and trace element redistribution). Metamorphic fluids in contact with crustal rocks are likely enriched in radiogenic Sr that will consistently modify the composition of apatite recrystallized during metamorphism. The Cenozoic apatite shows $Sr_{(i)}$ values that partly overlap or are higher than the seawater composition at the time (except for one measurement obtained on the Lower Oligocene sample STN2). These more radiogenic compositions could be due to the involvement of the third component as shown in Fig. 9C. This component would relate to trace elements released from Fe-oxyhydroxides – and other minerals constituting the sediment where apatite formed – to pore water. It is possible that these minerals possess a more crustal signature and therefore would have contributed with a more radiogenic Sr composition to the system during apatite formation (early diagenesis). The Sr isotope composition of apatite from the Late Cretaceous phosphatic calcarenite largely overlaps the range of contemporaneous seawater. The more radiogenic compositions – that are somewhat higher than seawater – were measured on pebbles that are inherited from slightly earlier (and possibly incomplete) phosphatization processes.

By contrast with most of their Sr isotope compositions, the O isotope signature of the Late Cretaceous and Cenozoic apatite overlaps with the seawater composition range. Similarly, their $\delta^{18}O$ is similar to contemporaneous phosphorites, marine fossils or fish debris and teeth that are not modified by late diagenetic alteration or weathering (see Fig. 7). This suggests that the investigated Late Cretaceous and Cenozoic apatite was not re-equilibrated isotopically with the interstitial water oxygen during diagenesis (e.g. McArthur *et al.*, 1986; Kastner *et al.*, 1990; Sharp *et al.*, 2000; Brand *et al.*, 2011) or modified by meteoric or hydrothermal waters/fluids (e.g. Longinelli *et al.*, 2002). Indeed, such processes would lead to a decrease in $\delta^{18}O$. By opposition, the O isotope composition of apatite from the Middle Cambrian deformed lenses/layers and Middle Ordovician nodules exhibits a shift towards lighter $\delta^{18}O$ compositions. This highlights the re-equilibration of

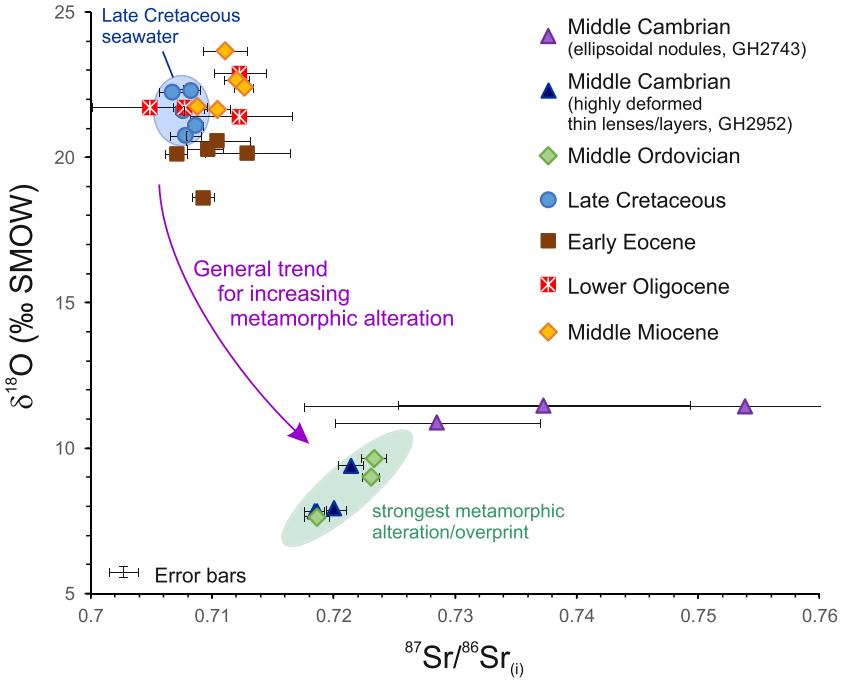

Fig. 10. Correlation between $^{87}Sr/^{86}Sr_{(i)}$ and $\delta^{18}O$ for apatite hosted in the different P-rich rocks from Belgium.

apatite with ^{18}O-depleted meteoric fluids circulating during or after the metamorphism. Interestingly, the O isotope composition of apatite from the Middle Cambrian ellipsoidal nodules, which are less affected by the deformation, is similar to the signature of apatite of the same age that are only altered by diagenetic processes (see data presented for comparison purposes, Fig. 7).

Considering both isotope systems and the previously considered geochemical features (see Figs 6 and 9; see sections *Late Cretaceous phosphorites* and *Further investigations about sources and post-depositional processes*), it appears that the Late Cretaceous apatite from the phosphatic chalk of the Mons Basin keeps the most pristine signature amidst the samples investigated. Cenozoic apatite records a slight shift in Sr isotope composition that would be related to pore water chemistry evolution during diagenesis (for instance, due to destabilization of aluminosilicates), as also attested to by the moderate modification of the REE patterns, and Ho/Y and ΣREE/Th ratios. The O isotope composition of this apatite is not modified. By contrast, apatite from the Middle Cambrian and Middle Ordovician P-rich rocks testify well to increasing effects of the metamorphism, considering both its Sr and O isotope compositions and its REE and trace element signatures (Figs 6 and 10).

SUMMARY AND CONCLUSIONS

This petrological, mineralogical, chemical and *in situ* isotope (Sr and O) study focused on phosphogenesis and processes leading to rare earth element (REE) concentration and (re-)distribution in apatite from P-rich rocks that are representative of major phosphogenic provinces dated to the Lower Palaeozoic, the Late Cretaceous and the Cenozoic. The chosen Belgian phosphate occurrences/deposits offer the opportunity to investigate the environment prevailing at the time of phosphogenesis, but also the importance of processes that controlled the chemistry of apatite after its deposition (and transport), as (late-)diagenesis and metamorphism.

In the Middle Cambrian turbiditic beds, fluorapatite [as confirmed by Raman spectra and electron micro-probe analyses (EMPA)] is present as ellipsoidal nodules or highly deformed layers/lenses, testifying to metamorphism and deformation. The less-deformed ellipsoidal nodules are characterized by a middle rare earth element (MREE) bulge in their REE patterns, which suggests the involvement of Fe-oxyhydroxides that retain or release trace elements to the pore water due to redox variations. A suboxic environment is inferred from these variations and is further confirmed by the lack of significant Ce

and Eu anomalies. Comparatively, in the more deformed lenses/layers, the REE patterns exhibit a loss in light rare earth elements (LREE) and heavy rare earth elements (HREE) and a marked positive Eu anomaly. The loss in REE is likely due to apatite recrystallization during deformation, and competition for REE with coeval monazite, xenotime and allanite. The positive Eu anomaly would indicate the influence of hydrothermal fluids in the system. Such a positive Eu anomaly is also observed in the REE patterns of fluorapatite from the Middle Ordovician conglomerate. It would similarly suggest the involvement of hot fluids during the metamorphism, which is obvious in these rocks where spessartine porphyroblasts are found as inclusions in fluorapatite. This is further supported by the very light oxygen isotopes measured on this apatite. By contrast with the Middle Cambrian apatite, the REE pattern of the Middle Ordovician apatite shows LREE enrichment, which could result from the recrystallization of apatite in parallel with the neoformation of spessartine, which is supposedly HREE-rich (Grauch, 1989). Preferential uptake of HREE in garnet would have left a fluid apparently enriched in LREE when apatite crystallized. Spessartine would form through the diffusion of Mn^{2+} in a primary P-rich mud. The involvement of a Mn^{2+}-enriched fluid is further supported by the bright green cathodoluminescence (CL) of apatite, the activation of which is related to divalent manganese (as shown in the CL spectrum). The shift towards lower $\delta^{18}O$ and radiogenic Sr-enriched isotope composition of Lower Palaeozoic apatite highlights interaction with $\delta^{18}O$-depleted meteoric fluids and a crustal component during the deformation phase. The latter is responsible for the variably intense recrystallization of apatite associated with a redistribution of the REE.

The phosphate grains and peloids of the Late Cretaceous phosphatic calcarenite from the Mons Basin are made of carbonate fluorapatite, as deduced from Raman spectra, EMPA analyses and CL. They present REE characteristics that are very close to the signature of the pore water at the bottom seawater–sediment interface, which is supposed to have experienced suboxic conditions. One of the most notable features of the REE patterns is the strong negative Ce anomaly that highlights the influence of oxygenated seawater. Although apatite presents a signature close to seawater, it is nevertheless affected by external addition of REE into the system and also a late diagenetic overprint that induced modification of the REE distribution. Conglomeratic beds at the edge of the Mons Basin contain carbonate fluorapatite pebbles that are more intensely phosphatized than the grains in the phosphatized calcareous matrix. This suggests multiple phosphogenic events and reworking/winnowing. Comparatively to the apatite grains in phosphatic calcarenite, the REE patterns of apatite pebbles show a one order of magnitude lower REE content and even more in MREE [attested by the higher $(La/Sm)_N$ and lower $(Gd/Yb)_N$, Table S3], which could indicate reworking from a source where phosphatization and/or REE enrichment was incomplete. The O and Sr isotope data acquired on Late Cretaceous apatite, whether it is in peloids or pebbles, largely overlap with the signature of the contemporaneous seawater.

The Cenozoic sub-rounded apatite nodules, reworked from P-rich beds, are made of carbonate fluorapatite, as confirmed by EMPA, CL and inferred from the absence of distinct peaks in the Raman spectra. Cenozoic apatite mostly presents flat REE patterns without any significant Ce and Eu anomalies. These features reflect a likely detrital influence and phosphogenesis in the oxic to suboxic zone during early diagenesis. Slight changes in REE distribution are assigned to post-depositional alteration. Contribution from pore water can also lead to a shift towards more radiogenic Sr isotope composition compared to seawater (with no significant shift in O isotope ratio with respect to seawater). This is likely if the pore water chemistry was previously modified by the destabilization of aluminosilicates during early diagenesis.

Combined Raman spectroscopy, cathodoluminescence, laser ablation – inductively coupled plasma – mass spectrometry (LA-ICP-MS) and *in situ* O and Sr isotope compositions are helpful to: (i) decipher the nature of apatite (here, crystalline fluorapatite versus crypto/microcrystalline carbonate fluorapatite); (ii) understand the succession of geological processes that led to the deposition of phosphate deposits and subsequently modify the chemistry (REE enrichment and distribution) of apatite; and (iii) gain more insight into the issue of element/fluid source in various settings of phosphogenesis. Oxygen isotope signature is seemingly more robust and less affected by (late) diagenetic alteration compared to Sr isotope ratios. In the future, it would be worth

using these tools more systematically to study apatite in phosphorites and investigate the genesis and possible potential regarding the REE of these deposits.

ACKNOWLEDGEMENTS

The authors would like to thank Alain Herbosch, Olivier Lambert and Etienne Steurbaut for having provided samples and crucial field information. Damien Jacquemin is thanked for his help in studying the phosphatic chalk of the Mons Basin. The authors are also grateful to Thommy D'heuvaert, Marleen DeCeukelaire and Thomas Goovaerts for the handling and preparation of samples from the collection of the RBINS. The GSB has received funding from the European Union's Horizon 2020 research and innovation program under grant agreement No 731166, through the project FRAME "Forecasting and assessing Europe's strategic raw materials needs". This work is also part of the GSEU – Geological Service for Europe project (through its WP2: Critical Raw Materials, the International Centre of Excellence and the United Nations Framework Classification), which has received funding from the European Union's Horizon Europe research and innovation programme under Grant Agreement. This work was partly done at the LA-ICP-MS laboratory of GeoRessources in Nancy which is funded by the Labex Ressources 21 (ANR-10-LABX-21-RESSOURCES21), the Région Lorraine and the European Community through the FEDER (European Regional Development Fund) program. The Cameca IMS 1280 HR2 ion microprobe at CRPG Nancy is an instrument of the LG-SIMS INSU CNRS national facility. The authors are grateful to Nathan Sheldon (Associate Editor), and an anonymous reviewer, for helpful remarks on the manuscript. Their comments have contributed to improve substantially the quality of this paper. Besides, they do thank Alex Brasier (Chief Editor) and Elaine Richardson (Journal Office Manager) for the handling of the manuscript.

DATA AVAILABILITY STATEMENT

The data that support the findings of this study are available from the corresponding author upon reasonable request.

REFERENCES

Álvaro, J.J., **Shields-Zhou, G.A.**, **Ahlberg, P.**, **Jensen, S.** and **Palacios, T.** (2016) Ediacaran–Cambrian phosphorites from the western margins of Gondwana and Baltica. *Sedimentology*, **63**, 350–377.

Antonakos, A., **Liarokapis, E.** and **Leventouri, T.** (2007) Micro-Raman and FTIR studies of synthetic and natural apatites. *Biomaterials*, **28**, 3043–3054.

Bach, W. and **Irber, W.** (1998) Rare earth element mobility in the oceanic lower sheeted dyke complex: evidence from geochemical data and leaching experiments. *Chem. Geol.*, **151**, 309–326.

Baele, J.M., **Papier, S.**, **Barriquant, L.** and **Barriquant, J.** (2011) Insight into the use of cathodoluminescence for bone taphonomy in the fossil bear deposit of Azé Cave, Saône-et-Loire, France. *Quaternaire*, **4**, 291–296.

Baele, J.M., **Decrée, S.** and **Rusk, B.** (2019) Cathodoluminescence applied to ore geology and exploration. In: *Ore Deposits: Origin, Exploration, and Exploitation* (Eds Decrée, S. and Robb, L.), pp. 131–161. Wiley, New York, NY.

Balson, P.S. (1980) The origin and evolution of Tertiary phosphorites from eastern England. *J. Geol. Soc. London*, **137**, 723–729.

Bassett, D., **Macleod, K.G.**, **Miller, J.F.** and **Ethington, R.L.** (2007) Oxygen isotopic composition of biogenic phosphate and the temperature of Early Ordovician seawater. *Palaios*, **22**, 98–103.

Bau, M. and **Dulski, P.** (1996) Distribution of yttrium and rare-earth elements in the Penge and Kuruman iron-formations, Transvaal Supergroup, South Africa. *Precambrian Res.*, **79**, 37–55.

Bau, M. and **Dulski, P.** (1999) Comparing yttrium and rare earths in hydrothermal fluids from the Mid-Atlantic Ridge: implications for Y and REE behaviour during near-vent mixing and for the Y/Ho ratio of Proterozoic seawater. *Chem. Geol.*, **155**, 77–90.

Bau, M., **Balan, S.**, **Schmidt, K.** and **Koschinsky, A.** (2010) Rare earth elements in mussel shells of the Mytilidae family as tracers for hidden and fossil high-temperature hydrothermal systems. *Earth Planet. Sci. Lett.*, **299**, 310–316.

Belousova, E.A., **Griffin, W.L.**, **O'Reilly, S.Y.** and **Fisher, N.I.** (2002) Apatite as an indicator mineral for mineral exploration: trace-element compositions and their relationship to host rock type. *J. Geochem. Explor.*, **76**, 45–69.

van den Bosch, M., **Cadee, M.C.** and **Janssen, A.W.** (1975) Lithostratigraphical and biostratigraphical subdivision of Tertiary deposits (Oligocene–Pliocene) in the Winterswijk-Almelo region (eastern part of The Netherlands). *Scripta Geol.*, **29**, 1–167.

Brand, U., **Logan, A.**, **Bitner, M.A.**, **Griesshaber, E.**, **Azmy, K.** and **Buhl, D.** (2011) What is the ideal proxy of Palaeozoic seawater chemistry? *Assoc. Australas. Paleontol. Mem.*, **41**, 9.

Brasier, M.D. (1980) The Lower Cambrian transgression and glauconite-phosphate facies in western Europe. *J. Geol. Soc. London*, **137**, 695–703.

Burke, W.H., **Denison, R.E.**, **Hetherington, E.A.**, **Koepnick, R.B.**, **Nelson, H.F.** and **Otto, J.B.** (1982) Variation of seawater 87Sr/86Sr throughout Phanerozoic time. *Geology*, **10**, 516–519.

Burnotte, E., **Pirard, E.** and **Michel, G.** (1989) Genesis of gray monazites; evidence from the Paleozoic of Belgium. *Econ. Geol.*, **84**, 1417–1429.

Byrne, R.H., **Liu, X.** and **Schijf, J.** (1996) The influence of phosphate coprecipitation on rare earth distributions in natural waters. *Geochim. Cosmochim. Acta*, **60**, 3341–3346.

Chakhmouradian, A.R., **Reguir, E.P.**, **Zaitsev, A.N.**, **Couëslan, C.**, **Xu, C.**, **Kynický, J.**, **Mumin, A.H.** and **Yang, P.** (2017) Apatite in carbonatitic rocks: Compositional variation, zoning, element partitioning and petrogenetic significance. *Lithos*, **274**, 188–213.

Chen, D., **Wang, J.**, **Qing, H.**, **Yan, D.** and **Li, R.** (2009) Hydrothermal venting activities in the Early Cambrian, South China: petrological, geochronological and stable isotopic constraints. *Chem. Geol.*, **258**, 168–181.

Chen, J., **Algeo, T.J.**, **Zhao, L.**, **Chen, Z.Q.**, **Cao, L.**, **Zhang, L.** and **Li, Y.** (2015) Diagenetic uptake of rare earth elements by bioapatite, with an example from Lower Triassic conodonts of South China. *Earth Sci. Rev.*, **149**, 181–202.

Chen, J., **Shen, S.Z.**, **Li, X.H.**, **Xu, Y.G.**, **Joachimski, M.M.**, **Bowring, S.A.**, **Erwin, D.H.**, **Yuan, D.X.**, **Chen, B.**, **Zhang, H.**, **Wang, Y.**, **Cao, C.Q.**, **Zheng, Q.F.** and **Mu, L.** (2016) High-resolution SIMS oxygen isotope analysis on conodont apatite from South China and implications for the end-Permian mass extinction. *Palaeogeogr. Palaeoclimatol. Palaeoecol.*, **448**, 26–38.

Condie, K.C. (1993) Chemical composition and evolution of the upper continental crust: contrasting results from surface samples and shales. *Chem. Geol.*, **104**, 1–37.

De Man, E. (2006) *Benthic Foraminifera Biofacies-Analysis and Stable Isotopes of the Middle Eocene to Oligocene Successions in the Southern North Sea Basin. Tools for Stratigraphy and for Reconstruction of the Extreme Climates*. PhD thesis. Katholieke Universiteit Leuven, Leuven, 250 p.

De Putter, T., **Charlet, J.M.** and **Quinif, Y.** (1999) REE, Y and U concentration at the fluid–iron oxide interface in late Cenozoic cryptodolines from Southern Belgium. *Chem. Geol.*, **153**, 139–150.

Debacker, T., **Sintubin, M.** and **Verniers, J.** (2002) Timing and duration of the progressive deformation of the Brabant Massif (Belgium). *Aardkundige Mededelingen*, **12**, 73–76.

Debacker, T.N., **Dewaele, S.**, **Sintubin, M.**, **Verniers, J.**, **Muchez, P.** and **Boven, A.** (2005) Timing and duration of the progressive deformation of the Brabant Massif, Belgium. *Geol. Belg*, **8**, 20–34.

Debacker, T.N., **Dumon, M.** and **Matthys, A.** (2009) Interpreting fold and fault geometries from within the lateral to oblique parts of slumps: a case study from the Anglo-Brabant Deformation Belt (Belgium). *J. Struct. Geol.*, **31**, 1525–1539.

Decrée, S., **Boulvais, P.**, **Tack, L.**, **André, L.** and **Baele, J.M.** (2016) Fluorapatite in carbonatite-related phosphate deposits: the case of the Matongo carbonatite (Burundi). *Miner. Deposita*, **51**, 453–466.

Decrée, S., **Ihlen, P.** and **Schiellerup, H.** (2017) Potential of phosphate deposits in Europe. *SGA News*, **41**, 14–20.

Decrée, S., **Cawthorn, G.**, **Deloule, E.**, **Mercadier, J.**, **Frimmel, H.** and **Baele, J.M.** (2020a) Unravelling the processes controlling apatite formation in the Phalaborwa Complex (South Africa) based on combined cathodoluminescence, LA-ICPMS and in situ O and Sr isotope analyses. *Contrib. Mineral. Petrol.*, **175**, 34.

Decrée, S., **Savolainen, M.**, **Mercadier, J.**, **Debaille, V.**, **Höhn, S.**, **Frimmel, H.** and **Baele, J.M.** (2020b) Geochemical and spectroscopic investigation of apatite in the Siilinjärvi Carbonatite Complex: keys to understanding apatite forming processes and assessing potential for REE. *J. Geochem. Explor.*, **123**, 104778.

Decrée, S., **Coint, N.**, **Debaille, V.**, **Hagen-Peter, G.**, **Leduc, T.** and **Schiellerup, H.** (2022a) Potential for REE of igneous-related apatite deposits in Europe. *J. Geol. Soc. London*, **526**, 219–249.

Decrée, S., **Pasava, J.**, **Baele, J.M.**, **Mercadier, J.**, **Rösel, D.** and **Frimmel, H.** (2022b) *In situ* trace element and Sr isotope signature of apatite: a new key to unravelling the genesis of polymetallic mineralisation in black shales (Early Cambrian Niutitang Formation, Southern China). *Ore Geol. Rev.*, **50**, 105–130.

Denison, R.E., **Koepnick, R.B.**, **Burke, W.H.** and **Hetherington, E.A.** (1998) Construction of the Cambrian and Ordovician seawater 87Sr/86Sr curve. *Chem. Geol.*, **152**, 325–340.

Drummond, J.B., **Pufahl, P.K.**, **Porto, C.G.** and **Carvalho, M.** (2015) Neoproterozoic peritidal phosphorite from the Sete Lagoas Formation (Brazil) and the Precambrian phosphorus cycle. *Sedimentology*, **62**, 1978–2008.

Edwards, C.T., **Jones, C.M.**, **Quinton, P.C.** and **Fike, D.A.** (2022) Oxygen isotope (δ18O) trends measured from Ordovician conodont apatite using secondary ion mass spectrometry (SIMS): Implications for paleo-thermometry studies. *GSA Bull.*, **134**, 261–274.

Elderfield, H. and **Greaves, M.J.** (1982) The rare earth elements in seawater. *Nature*, **296**, 214–219.

Elderfield, H., **Upstill-Goddard, R.** and **Sholkovitz, E.R.** (1990) The rare earth elements in rivers, estuaries, and coastal seas and their significance to the composition of ocean waters. *Geochim. Cosmochim. Acta*, **54**, 971–991.

Elrick, M., **Rieboldt, S.**, **Saltzman, M.** and **McKay, R.M.** (2011) Oxygen-isotope trends and seawater temperature changes across the Late Cambrian Steptoean positive carbon-isotope excursion (SPICE event). *Geology*, **39**, 987–990.

Emo, R.B., **Smit, M.A.**, **Schmitt, M.**, **Kooijman, E.**, **Scherer, E.E.**, **Sprung, P.**, **Bleeker, W.** and **Mezger, K.** (2018) Evidence for evolved Hadean crust from Sr isotopes in apatite within Eoarchean zircon from the Acasta Gneiss Complex. *Geochim. Cosmochim. Acta*, **235**, 450–462.

Emsbo, P., **McLaughlin, P.I.**, **Breit, G.N.**, **du Bray, E.A.** and **Koenig, A.E.** (2015) Rare earth elements in sedimentary phosphate deposits: solution to the global REE crisis? *Gondw. Res.*, **27**, 776–785.

Fielitz, W. and **Mansy, J.L.** (1999) Pre-and synorogenic burial metamorphism in the Ardenne and neighbouring areas (Rhenohercynian zone, central European Variscides). *Tectonophysics*, **309**, 227–256.

Flicoteaux, R. and **Trompette, R.** (1998) Cratonic and foreland Early Cambrian phosphorites of West Africa: Palaeoceanographical and climatical contexts. *Palaeogeogr. Palaeoclimatol. Palaeoecol.*, **139**, 107–120.

Föllmi, K.B. (1996) The phosphorus cycle, phosphogenesis and marine phosphate-rich deposits. *Earth Sci. Rev.*, **40**, 55–124.

Franssen, L. and **Michot, J.** (1969) Etude pétrographique du sondage de Grand Halleux. *Ann. Soc. Géol. Belg*, **92**, 229–240.

Gao, P., **He, Z.**, **Li, S.**, **Lash, G.G.**, **Li, B.**, **Huang, B.** and **Yan, D.** (2018) Volcanic and hydrothermal activities recorded in phosphate nodules from the Lower Cambrian Niutitang Formation black shales in South China. *Palaeogeogr. Palaeoclimatol. Palaeoecol.*, **505**, 381–397.

Geological Survey of Belgium. (1996) Simplified geological map of Belgium, 1 sheet.

Geukens, F. (1999) Notes accompagnant une révision de la carte structurale du Massif de Stavelot. *Aardkundige Mededelingen*, **9**, 183–190.

Goldoff, B., **Webster, J.D.** and **Harlov, D.E.** (2012) Characterization of fluor-chlorapatites by electron probe microanalysis with a focus on time-dependent intensity variation of halogens. *Am. Mineral.*, **97**, 1103–1115.

Grauch, R.I. (1989) Rare earth elements in metamorphic rocks. *Rev. Mineral. Geochem.*, **21**, 147–167.

Graulich, J.M. (1980) Le sondage de Grand-Halleux. *Serv. Géol. Belg. Pap. Prof.*, **175**, 84.

Hannisdal, B. and **Peters, S.E.** (2011) Phanerozoic Earth system evolution and marine biodiversity. *Science*, **334**, 1121–1124.

Harlov, D.E. and **Förster, H.J.** (2003) Fluid-induced nucleation of (Y+ REE)-phosphate minerals within apatite: Nature and experiment. Part II. Fluorapatite. *Am. Mineral.*, **88**, 1209–1229.

Henrichs, I.A., **Chew, D.M.**, **O'Sullivan, G.J.**, **Mark, C.**, **McKenna, C.** and **Guyett, P.** (2019) Trace element (Mn-Sr-Y-Th-REE) and U-Pb isotope systematics of metapelitic apatite during progressive greenschist- to amphibolite-facies barrovian metamorphism. *Geochem. Geophys. Geosyst.*, **20**, 4103–4129.

Herbosch, A. (2021) Stratigraphic correlations between the Brabant Massif and the Stavelot, Rocroi and Givonne inliers (Belgium) and geological implications To Michel Vanguestaine, with my respect for his outstanding pioneering work. *Geol. Belg.*, **24**, 137–157.

Herbosch, A. and **Verniers, J.** (2011) What is the biostratigraphic value of the ichnofossil Oldhamia for the Cambrian: a review. *Geol. Belg.*, **14**, 229–248.

Herbosch, A. and **Verniers, J.** (2014) Stratigraphy of the Lower Palaeozoic of the Brabant Massif, Belgium. Part II: The Middle Ordovician to lowest Silurian of the Rebecq Group. *Geol. Belg.*, **17**, 115–136.

Herbosch, A., **Liégeois, J.P.** and **Pin, C.** (2016) Coticules of the Belgian type area (Stavelot-Venn Massif): Limy turbidites within the nascent Rheic oceanic basin. *Earth Sci. Rev.*, **159**, 186–214.

Herbosch, A., **Liégeois, J.P.**, **Gärtner, A.**, **Hofmann, M.** and **Linnemann, U.** (2020) The Stavelot-Venn Massif (Ardenne, Belgium), a Rift Shoulder Basin Ripped off the West African Craton: Cartography, stratigraphy, sedimentology, new U-Pb on zircon ages, geochemistry and Nd isotopes evidence. *Earth-Sci. Rev.*, **20**, 103142.

Herwartz, D., **Tütken, T.**, **Jochum, K.P.** and **Sander, P.M.** (2013) Rare earth element systematics of fossil bone revealed by LA-ICPMS analysis. *Geochim. Cosmochim. Acta*, **103**, 161–183.

von Hoegen, J., **Lemme, B.**, **Zielinski, J.** and **Walter, R.** (1985) Cambrian and Lower Ordovician in the Stavelot-Venn Massif. A model for depositional history. *Neues Jb. Geol. Paläontol. Abh.*, **171**, 217–235.

Iserbyt, A. and **De Schutter, P.J.** (2012) Quantitative analysis of Elasmobranch assemblages from two successive Ypresian (early Eocene) facies at Marke, western Belgium. *Geol. Belg.*, **15**, 146–153.

Jacquemin, D. (2020) The phosphatic chalk of the Mons Basin, Belgium. Petrography and geochemistry of the Ciply Phosphatic Chalk and implications on its genesis. *Geol. Surv. Belg. Mem.*, **64**, 82.

Jarvis, I. (1992) Sedimentology, geochemistry and origin of phosphatic chalks: the Upper Cretaceous deposits of NW Europe. *Sedimentology*, **39**, 55–97.

Jarvis, I. (1994) Phosphorite geochemistry: state-of-the-art and environmental concerns. *Eclogae Geol. Helv.*, **87**, 643–700.

Jarvis, I. (2006) The Santonian-Campanian phosphatic chalks of England and France. *Proc. Geol. Assoc.*, **117**, 219–237.

Jochum, K.P., **Weis, U.**, **Stoll, B.**, **Kuzmin, D.**, **Yang, Q.**, **Raczek, I.**, **Jacob, D.E.**, **Stracke, A.**, **Birbaum, K.**, **Frick, D.A.**, **Günther, D.** and **Enzweiler, J.** (2011) Determination of reference values for NIST SRM 610–617 glasses following ISO guidelines. *Geostand. Geoanal. Res.*, **35**, 397–429.

Kastner, M., **Garrison, R.E.**, **Kolodny, Y.**, **Reimers, C.E.** and **Shemesh, A.** (1990) Coupled changes of oxygen isotopes in PO_4 and CO_3 in apatite, with emphasis on the Monterey Formation, California. In: *Phosphate Deposits of the World, Vol. 3, Neogene to Modern Phosphorites* (Eds Burnett, W.C. and Riggs, S.R.), pp. 312–324. Cambridge University Press, Cambridge.

Kempe, U. and **Götze, J.** (2002) Cathodoluminecence (CL) behaviour and crystal chemistry of apatite from rare-metal deposits. *Mineral. Mag.*, **66**, 151–172.

Kidder, D.L., **Krishnaswamy, R.** and **Mapes, R.H.** (2003) Elemental mobility in phosphatic shales during concretion growth and implications for provenance analysis. *Chem. Geol.*, **198**, 335–353.

Kocsis, L., **Ősi, A.**, **Vennemann, T.**, **Trueman, C.N.** and **Palmer, M.R.** (2009a) Geochemical study of vertebrate fossils from the Upper Cretaceous (Santonian) Csehbánya Formation (Hungary): Evidence for a freshwater habitat of mosasaurs and pycnodont fish. *Palaeogeogr. Palaeoclimatol. Palaeoecol.*, **280**, 532–542.

Kocsis, L., **Vennemann, T.W.**, **Hegner, E.**, **Fontignie, D.** and **Tütken, T.** (2009b) Constraints on Miocene oceanography and climate in the Western and Central Paratethys: O-, Sr-, and Nd-isotope compositions of marine fish and mammal remains. *Palaeogeogr. Palaeoclimatol. Palaeoecol.*, **271**, 117–129.

Koepnick, R.B., **Burke, W.H.**, **Denison, R.E.**, **Hetherington, E.A.**, **Nelson, H.F.**, **Otto, J.B.** and **Waite, L.E.** (1985) Construction of the seawater $^{87}Sr/^{86}Sr$ curve for the Cenozoic and Cretaceous: supporting data. *Chem. Geol.*, **58**, 55–81.

Kohn, M.J. and **Cerling, T.E.** (2002) Stable Isotope Compositions of Biological Apatite. Phosphates-Geochemical, Geobiological, and Materials Importance. *Rev. Mineral. Geochem.*, **20**, 455–488.

Krajewski, K.P., **Cappellen, P.V.**, **Trichet, J.**, **Kuhn, O.**, **Lucas, J.** and **Martin-Algarra, A.** (1994) Biological processes and apatite formation in sedimentary environments. *Eclogae Geol. Helv.*, **87**, 701–746.

Lécuyer, C., **Grandjean, P.**, **O'Neil, J.R.**, **Cappetta, H.** and **Martineau, F.** (1993) Thermal excursions in the ocean at the Cretaceous—Tertiary boundary (northern Morocco): $\delta^{18}O$ record of phosphatic fish debris. *Palaeogeogr. Palaeoclimatol. Palaeoecol.*, **105**, 235–243.

Lécuyer, C., **Reynard, B.** and **Grandjean, P.** (2004) Rare earth element evolution of Phanerozoic seawater recorded in biogenic apatites. *Chem. Geol.*, **204**, 63–102.

Li, Z., **Duan, D.**, **Jiang, S.**, **Ma, Y.** and **Yuan, H.** (2018) *In situ* analysis of major elements, trace elements and Sr isotopic compositions of apatite from the granite in the Chengchao skarn-type Fe deposit, Edong ore district: Implications for petrogenesis and mineralization. *J. Earth Sci.*, **29**, 295–306.

Linnemann, U., **Herbosch, A.**, **Liégeois, J.P.**, **Pin, C.**, **Gärtner, A.** and **Hofmann, M.** (2012) The Cambrian to Devonian odyssey of the Brabant Massif within Avalonia:

A review with new zircon ages, geochemistry, Sm–Nd isotopes, stratigraphy and palaeogeography. *Earth Sci. Rev.*, **112**, 126–154.

Longerich, H.P., **Jackson, S.E.** and **Günther, D.** (1996) Inter-laboratory note. Laser ablation inductively coupled plasma mass spectrometric transient signal data acquisition and analyte concentration calculation. *J. Anal. At. Spectrom*, **11**, 899–904.

Longinelli, A., **Iacumin, P.** and **Ramigni, M.** (2002) $\delta^{18}O$ of carbonate, quartz and phosphate from belemnite guards: implications for the isotopic record of old fossils and the isotopic composition of ancient seawater. *Earth Planet. Sci. Lett.*, **203**, 445–459.

Louwye, S. (2002) Dinoflagellate cyst biostratigraphy of the Upper Miocene Deurne Sands (Diest Formation) of northern Belgium, southern North Sea Basin. *Geol. J.*, **37**, 55–67.

Louwye, S. (2005) The Early and Middle Miocene transgression at the southern border of the North Sea Basin (northern Belgium). *Geol. J.*, **40**, 441–456.

Louwye, S., **Marquet, R.**, **Bosselaers, M.** and **Lambert, O.** (2010) Stratigraphy of an Early–Middle Miocene sequence near Antwerp in northern Belgium (southern North Sea basin). *Geol. Belg.*, **13**, 269–284.

Lovell, J.P.B. (1986) Cenozoic. In: *Introduction to the Petroleum Geology of the North Sea* (Ed. Glennie, K.W.), pp. 179–196. Blackwell Scientific Publications, London.

Lucas, J. and **Prévôt-Lucas, L.** (1995) Tethyan phosphates and bioproductites. In: *The Oceans Basins and Margins. The Tethys Ocean, Vol. 8* (Ed. Naim, A.E.M.), pp. 367–391. Plenum Press, New York, NY.

Lumiste, K., **Mänd, K.**, **Bailey, J.**, **Paiste, P.**, **Lang, L.**, **Lepland, A.** and **Kirsimäe, K.** (2019) REE+Y uptake and diagenesis in recent sedimentary apatites. *Chem. Geol.*, **525**, 268–281.

MacRae, N.D., **Nesbitt, H.W.** and **Kronberg, B.I.** (1992) Development of a positive Eu anomaly during diagenesis. *Earth Planet. Sci. Lett.*, **109**, 585–591.

de Magnée, I. and **Lambeau, J.** (1965) Le grés poudingue phosphatifère et manganesifère de Thy (Vallée de Dyle). *Bull. Soc. Belg.Géol. Paléontol. Hydrol.*, **74**, 293–300.

Marks, M.A., **Wenzel, T.**, **Whitehouse, M.J.**, **Loose, M.**, **Zack, T.**, **Barth, M.**, **Worgard, L.**, **Krasz, V.**, **Eby, G.N.**, **Stosnach, H.** and **Markl, G.** (2012) The volatile inventory (F, Cl, Br, S, C) of magmatic apatite: An integrated analytical approach. *Chem. Geol.*, **291**, 241–255.

Marquet, R. and **Herman, J.** (2012) Reinvestigation of the invertebrate fauna of the Boom Clay Formation and the Ruisbroek Sand Member (Oligocene, Rupelian) of Belgium, with the description of a new lithostratigraphic unit: the Sint Niklaas Phosphorite Bed. *Cainozoic Res.*, **9**, 101–120.

Martin, E.E. and **Haley, B.A.** (2000) Fossil fish teeth as proxies for seawater Sr and Nd isotopes. *Geochim. Cosmochim. Acta*, **64**, 835–847.

McArthur, J.M. (1985) Francolite geochemistry—compositional controls during formation, diagenesis, metamorphism and weathering. *Geochim. Cosmochim. Acta*, **49**, 23–35.

McArthur, J.M. and **Herczeg, A.** (1990) Diagenetic stability of the isotopic composition of phosphate-oxygen: palaeoenvironmental implications. *J. Geol. Soc. London, Spec Public*, **52**, 119–124.

McArthur, J.M. and **Walsh, J.N.** (1984) Rare-earth geochemistry of phosphorites. *Chem. Geol.*, **47**, 191–220.

McArthur, J.M., **Benmore, R.A.**, **Coleman, M.L.**, **Soldi, C.**, **Yeh, H.W.** and **O'Brien, G.W.** (1986) Stable isotopic characterisation of francolite formation. *Earth Planet. Sci. Lett.*, **77**, 20–34.

McClellan, G.H. and **Van Kauwenbergh, S.J.** (1991) Mineralogical and chemical variation of francolites with geological time. *J. Geol. Soc. London*, **148**, 809–812.

Michot, P. (1980) Le segment calédonien belge. Mémoire de la Classe des Sciences. *Acad. Roy. Belg. Mem.*, Collection in-8° - 2^{e} serie, Fascicule 6, 57 p.

Nothdurft, L.D., **Webb, G.E.** and **Kamber, B.S.** (2004) Rare earth element geochemistry of Late Devonian reefal carbonates, Canning Basin, Western Australia: confirmation of a seawater REE proxy in ancient limestones. *Geochim. Cosmochim. Acta*, **68**, 263–283.

Notholt, A.J. (1980) Economic phosphatic sediments: mode of occurrence and stratigraphical distribution. *J. Geol. Soc. London*, **137**, 793–805.

Notholt, A.J.G. and **Brasier, M.D.** (1986) Proterozoic and Cambrian phosphorites–regional review. Europe. In: *Phosphate Deposits of the World. Vol. 1. Proterozoic and Cambrian Phosphorites* (Ed. Cook, P.J.), pp. 91–100. Cambridge University Press, Cambridge.

Notholt, A.J.G. and **Sheldon, R.P.** (1986) Proterozoic and Cambrian phosphorites—regional review: World resources. In: *Phosphate Deposits of the World. Vol. 1. Proterozoic and Cambrian Phosphorites* (Ed. Cook, P.J.), pp. 9–19. Cambridge University Press, Cambridge.

Nutman, A.P. (2007) Apatite recrystallisation during prograde metamorphism, Coosma, southeast Australia: implications for using an apatite–graphite association as a biotracer in ancient metasedimentary rocks. *Australian J. Earth Sci.*, **54**, 1023–1032.

Ounis, A., **Kocsis, L.**, **Chaabani, F.** and **Pfeifer, H.R.** (2008) Rare earth elements and stable isotope geochemistry ($\delta^{13}C$ and $\delta^{18}O$) of phosphorite deposits in the Gafsa Basin, Tunisia. *Palaeogeogr. Palaeoclimatol. Palaeoecol.*, **268**, 1–18.

Parrish, J.T. (1990) Paleogeographic and paleoclimatic setting of the Miocene phosphogenic episode. In: *Phosphate Deposits of the World, Vol. 3, Genesis of Neogene to Recent Phosphorites* (Eds Burnett, W.C. and Riggs, S.R.), pp. 223–240. Cambridge University Press, Cambridge.

Parrish, J.T., **Ziegler, A.M.**, **Scotese, C.R.** and **Humphreyville, L.** (1986) Proterozoic and Cambrian Phosphorites – Specialist Studies: Early Cambrian palaeogeogaphy, palaeoceanography, and phosphorites. In: *Phosphate Deposits of the World, Vol. 1, Proterozoic and Cambrian Phosphorites* (Eds Cook, P.J. and Shergold, J.H.), pp. 280–294. Cambridge University Press, Cambridge.

Paton, C., **Hellstrom, J.**, **Paul, B.**, **Woodhead, J.** and **Hergt, J.** (2011) Iolite: Freeware for the visualisation and processing of mass spectrometric data. *J. Anal. At. Spectrom*, **26**, 2508–2518.

Penel, G., **Leroy, G.**, **Rey, C.**, **Sombret, B.**, **Huvenne, J.P.** and **Bres, E.** (1997) Infrared and Raman microspectrometry study of fluor-fluor-hydroxy and hydroxy-apatite powders. *J. Mater. Sci.*, **8**, 271–276.

Piessens, K. and **Sintubin, M.** (1997) Partitioning of the variscan strain in the southern part of the Caledonina Stavelot-Venn Inlier in the Ardenne Allochthon (Belgium). *Aardkundige Mededelingen*, **8**, 135–138.

Potts, P.J. and **Tindle, A.G.** (1989) Analytical characteristics of a multilayer dispersion element (2d=60Å) in the determination of fluorine in minerals by electron microprobe. *Mineral. Mag.*, **53**, 357–362.

Pufahl, P.K. and **Grimm, K.A.** (2003) Coated phosphate grains: Proxy for physical, chemical, and ecological changes in seawater. *Geology*, **31**, 801–804.

Pufahl, P.K. and **Groat, L.A.** (2017) Sedimentary and igneous phosphate deposits: formation and exploration: an invited paper. *Econ. Geol.*, **112**, 483–516.

Quinif, Y., **Vandycke, S.** and **Vergari, A.** (1997) Chronologie et causalite entre tectonique et karstification; l'exemple des paleokarsts du Hainaut (Belgique). *Bull.Soc. Géol. Fr.*, **168**, 463–472.

Quinton, P.C., **Law, S.**, **Macleod, K.G.**, **Herrmann, A.D.**, **Haynes, J.T.** and **Leslie, S.A.** (2017) Testing the early Late Ordovician cool-water hypothesis with oxygen isotopes from conodont apatite. *Geol. Mag.*, **155**, 1727–1741.

Riggs, S.R. (1984) Paleoceanographic model of Neogene phosphorite deposition, US Atlantic continental margin. *Science*, **223**, 123–131.

Riggs, S.R. and **Sheldon, R.P.** (1990) Paleoceanographic and paleoclimatic controls of the temporal and geographic distribution of Upper Cenozoic continental margin sediments. In: *Phosphate Deposits of the World, Vol. 1, Proterozoic and Cambrian Phosphorites* (Eds Cook, P.J. and Shergold, J.H.), pp. 53–61. Cambridge University Press, Cambridge.

Robaszynski, F. and **Martin, M.** (1988) Late Cretaceous phosphate stratiform deposits of the Mons Basin (Belgium). In: *Mineral Deposits within the European Community* (Eds Boissonnas, J. and Omenetto, P.), pp. 515–529. Springer, Berlin, Heidelberg.

Schreyer, W., **Bernhardt, H.J.** and **Medenbach, O.** (1992) Petrologic evidence for a rhodochrosite precursor of spessartine in coticules of the Venn-Stavelot Massif, Belgium. *Mineral. Mag*, **56**, 527–532.

Schulz, H. and **Schulz, H.N.** (2005) Large sulfur bacteria and the formation of phosphorite. *Science*, **80**, 416–418.

Sharp, Z.D., **Atudorei, V.** and **Furrer, H.** (2000) The effect of diagenesis on oxygen isotope ratios of biogenic phosphates. *Amer. J. Sci.*, **300**, 222–237.

Shibata, S.N., **Tanaka, T.** and **Yamamoto, K.** (2006) Crystal structure control of the dissolution of rare earth elements in water-mineral interactions. *Geochem. J.*, **40**, 437–446.

Shields, G. and **Stille, P.** (2001) Diagenetic constraints on the use of cerium anomalies as palaeoseawater redox proxies: an isotopic and REE study of Cambrian phosphorites. *Chem. Geol.*, **175**, 29–48.

Shields, G. and **Webb, G.** (2004) Has the REE composition of seawater changed over geological time? *Chem. Geol.*, **204**, 103–107.

Sholkovitz, E.R., **Piepgras, D.J.** and **Jacobsen, S.B.** (1989) The pore water chemistry of rare earth elements in Buzzards Bay sediments. *Geochim. Cosmochim. Acta*, **53**, 2847–2856.

Spear, F.S. and **Pyle, J.M.** (2002) Apatite, monazite, and xenotime in metamorphic rocks. *Rev. Mineral. Geochem.*, **48**, 293–335.

Steurbaut, E. (1986) Late Middle Eocene to Middle Oligocene calcareous nannoplankton from the Kallo well, some boreholes and exposures in Belgium and a description of the Ruisbroek Sand Member. *Mededelingen van de Werkgroep voor Tertiaire en Kwartaire Geologie*, **23**, 49–83.

Stormer, J.C., **Pierson, M.L.** and **Tacker, R.C.** (1993) Variation of F and Cl X-ray intensity due to anisotropic diffusion in apatite during electron microprobe analysis. *Am. Mineral.*, **78**, 641–648.

Sun, Y., **Wiedenbeck, M.**, **Joachimski, M.M.**, **Beier, C.**, **Kemner, F.** and **Weinzierl, C.** (2016) Chemical and oxygen isotope composition of gem-quality apatites: implications for oxygen isotope reference materials for secondary ion mass spectrometry (SIMS). *Chem. Geol.*, **440**, 164–178.

Trappe, J. (2001) *Phanerozoic Phosphorite Depositional Systems: A Dynamic Model for a Sedimentary Resource System, Vol. 76*. Springer, Berlin, Heidelberg, 316 p.

Trotter, J.A., **Williams, I.S.**, **Barnes, C.R.**, **Lécuyer, C.** and **Nicoll, R.S.** (2008) Did cooling oceans trigger Ordovician biodiversification? Evidence from conodont thermometry. *Science*, **321**, 550–554.

Tuschel, D. (2017) Why are the Raman spectra of crystalline and amorphous solids different. *Spectroscopy*, **32**, 26–33.

Van Grootel, G., **Verniers, J.**, **Geerkens, B.**, **Laduron, D.**, **Verhaeren, M.**, **Hertogen, J.** and **De Vos, W.** (1997) Timing of magmatism, foreland basin development, metamorphism and inversion in the Anglo-Brabant fold belt. *Geol. Mag.*, **134**, 607–616.

Van Marcke, P., **Laenen, B.** and **Wouters, L.** (2005) *The Ypresian Clays as Possible Host Rock for Radioactive Waste Disposal: An Evaluation*. ONDRAF/NIRAS, Brussel.

Vandenberghe, N., **Brinkhuis, H.** and **Steurbaut, E.** (2003) The Eocene/Oligocene boundary in the North Sea area: a sequence stratigraphic approach. In: *From Greenhouse to Icehouse. The Marine Eocene-Oligocene Transition* (Eds Prothero, D.D., Ivany, L.C. and Nesbitt, E.A.), pp. 419–437. Columbia University Press, New York, NY.

Veizer, J., **Ala, D.**, **Azmy, K.**, **Bruckschen, P.**, **Buhl, D.**, **Bruhn, F.**, **Carden, G.A.F.**, **Diener, A.**, **Ebneth, S.**, **Godderis, Y.**, **Jasper, T.**, **Korte, C.**, **Pawellek, F.**, **Podlaha, O.G.** and **Strauss, H.** (1999) $^{87}Sr/^{86}Sr$, $\delta^{13}C$ and $\delta^{18}O$ evolution of Phanerozoic seawater. *Chem. Geol.*, **161**, 59–88.

Verniers, J., **Herbosch, A.**, **Vanguestaine, M.**, **Geukens, F.**, **Delcambre, B.**, **Pingot, J.L.**, **Belanger, I.**, **Hennebert, M.**, **Debacker, T.**, **Sintubin, M.** and **De Vos, W.** (2001) Cambrian-Ordovician-Silurian lithostratigraphic units (Belgium). *Geol. Belg.*, **2001**, 5–38.

Waychunas, G.A. (2002) Apatite luminescence. In: *Reviews in Mineralogy and Geochemistry, Vol. 48 – Phosphates* (Eds Kohn, M.J., Rakovan, J. and Hughes, J.M.), pp. 701–742. Mineralogical Society of America, Washington, DC.

Wotte, T., **Skovsted, C.B.**, **Whitehouse, M.J.** and **Kouchinsky, A.** (2019) Isotopic evidence for temperate oceans during the Cambrian Explosion. *Nature Sci. Rep.*, **9**, 1–9.

Yang, Y.H., **Wu, F.Y.**, **Yang, J.H.**, **Chew, D.M.**, **Xie, L.W.**, **Chu, Z.Y.**, **Zhang, Y.B.** and **Huang, C.** (2014) Sr and Nd isotopic compositions of apatite reference materials used in U–Th–Pb geochronology. *Chem. Geol.*, **385**, 35–55.

Yang, J.H., **Kang, L.F.**, **Peng, J.T.**, **Zhong, H.**, **Gao, J.F.** and **Liu, L.** (2018) In situ elemental and isotopic compositions of apatite and zircon from the Shuikoushan and Xihuashan granitic plutons: Implication for Jurassic granitoid-related Cu-Pb-Zn and W mineralization in the Nanling Range, South China. *Ore Geol. Rev.*, **93**, 382–403.

Yang, Q., **Xia, X.P.**, **Zhang, L.**, **Zhang, W.**, **Zhang, Y.**, **Chen, L.**, **Yang, Y.** and **He, M.** (2020) Oxygen isotope homogeneity assessment for apatite U-Th-Pb geochronology reference materials. *Surf. Interf. Anal.*, **52**, 197–213.

Ye, Y., **Wang, H.**, **Wang, X.**, **Zhai, L.**, **Wu, C.** and **Zhang, S.** (2020) Elemental geochemistry of lower Cambrian phosphate nodules in Guizhou Province, South China: An integrated study by LA-ICP-MS mapping and solution ICP-MS. *Palaeogeogr. Palaeoclimatol. Palaeoecol.*, **538**, 109459.

Zeng, L.P., **Zhao, X.F.**, **Li, X.C.**, **Hu, H.** and **McFarlane, C.** (2016) In situ elemental and isotopic analysis of fluorapatite from the Taocun magnetite-apatite deposit, Eastern China: Constraints on fluid metasomatism. *Am. Mineral.*, **101**, 2468–2483.

Zhu, B., **Jiang, S.Y.**, **Yang, J.H.**, **Pi, D.**, **Ling, H.F.** and **Chen, Y.Q.** (2014) Rare earth element and Sr-Nd isotope geochemistry of phosphate nodules from the lower Cambrian Niutitang Formation, NW Hunan Province, South China. *Palaeogeogr. Palaeoclimatol. Palaeoecol.*, **398**, 132–143.

Žigaitė, Ž. and **Whitehouse, M.** (2014) Stable oxygen isotopes of dental biomineral: differentiation at the intra- and inter-tissue level of modern shark teeth. *Geol. Fören. Stockh. Förh.*, **136**, 337–340.

Manuscript received 7 December 2022; revision accepted 13 November 2023

Supporting Information

Additional information may be found in the online version of this article:

Table S1. Detailed description of the examined P-rich rocks from Belgium.

Table S2. Representative microprobe analyses (oxides in wt.%) of apatite from the P-rich rocks. The considered detection limit is 0.05 wt.%; (–) in the table correspond to analyses below detection limit. The formulae are calculated to 12.5 O.

Table S3. Rare earth element (REE) and trace element contents (in ppm), ΣREE contents, $(La/Sm)_N$, $(Gd/Yb)_N$, $(La/Yb)_N$, Ce/Ce*, Eu*/Eu and Pr/Pr* ratios of apatite from the P-rich rocks (LA-ICP-MS analyses).

Table S4. Sr and O isotopic data of apatite from the studied P-rich rocks (SIMS analyses).